Weierstraß-Institut
für Angewandte Analysis und Stochastik
Leibniz-Institut im Forschungsverbund Berlin e. V.

Preprint ISSN 2198-5855

Simulation of multi-frequency-induction-hardening including phase transitions and mechanical effects

Dietmar Hömberg[1], Qingzhe Liu[2], Jonathan Montalvo-Urquizo[3], Dawid Nadolski[4], Thomas Petzold[1], Alfred Schmidt[5], Alwin Schulz[4]

submitted: June 25, 2014

[1] Weierstraß–Institut
Mohrenstr. 39
10117 Berlin
Germany
E-Mail: dietmar.hoemberg@wias-berlin.de
thomas.petzold@wias-berlin.de

[2] Institut für Mathematik und Informatik
Ernst Moritz Arndt Universität
Walther-Rathenau-Straße 47
17487 Greifswald
Germany
E-Mail: liuq@uni-greifswald.de

[3] CIMAT-Monterrey
Campus de la Salud, UANL
Monterrey, Nuevo Leon
Mexico
E-Mail: jonathan.montalvo@cimat.mx

[4] Stiftung Institut für Werkstofftechnik IWT
Badgasteiner Str. 3
28359 Bremen
Germany
E-Mail: nadolski@iwt-bremen.de
aschulz@iwt-bremen.de

[5] Zentrum für Technomathematik
Universität Bremen
28334 Bremen
Germany
E-Mail: schmidt@math.uni-bremen.de

No. 1975
Berlin 2014

2010 *Mathematics Subject Classification.* 35K55, 35Q60, 74F05, 74F15.

Key words and phrases. Induction surface hardening, multi field problem, thermomechanics, TRIP, finite element simulation.

The authors gratefully acknowledge the financial support by the german federal ministry of education and research, BMBF. Furthermore, we thank EFD Induction and Dr. H. Stiele for the technical support and for providing experimental results.

Edited by
Weierstraß-Institut für Angewandte Analysis und Stochastik (WIAS)
Leibniz-Institut im Forschungsverbund Berlin e. V.
Mohrenstraße 39
10117 Berlin
Germany

Fax: +49 30 2044975
E-Mail: preprint@wias-berlin.de
World Wide Web: http://www.wias-berlin.de/

ABSTRACT. Induction hardening is a well known method for the heat treatment of steel components. With the concept of multi-frequency hardening, where currents with two different frequency components are provided on a single inductor coil, it is possible to optimize the hardening zone to follow a given contour even in the case of complicated 3D geometries like gears.

In this article, we consider the simulation of multi-frequency induction hardening in 3D. The equations to solve are the vector potential formulation of Maxwell's equations describing the electromagnetic fields, the balance of momentum to determine internal stresses and deformations arising from thermoelasticity and transformation induced plasticity, a rate law to determine the distribution of different phases and the heat equation to determine the temperature distribution in the workpiece.

The equations are solved using adaptive finite element methods. The simulation results are compared to experiments for discs and for gears. A very good agreement for the hardening profile and the temperature is observed. It is also possible to predict the distribution of residual stresses after the heat treatment.

1. INTRODUCTION

For many years surface hardening has been a well known method for enhancing the mechanical and tribological properties of components made from steel. This enhancement originates from the compressive residual stress which is generated when the surface layer has transformed into martensite and from the hardness of the martensite itself.

The benefit of using electromagnetic induction for surface hardening in comparison to other heating technologies is that the heating energy is provided directly inside the surface areas of the workpiece. This is advantageous with regard to energy consumption and production flow.

On the other hand, the induction hardening process is influenced by an enormous number of basic and secondary conditions and parameters, respectively. First of all, the workpiece itself, i.e. its material and shape, affects the process by influencing the electromagnetic field. Secondly, the shape of the field generating inductor coil and its distance to the workpiece surface strongly influence the energy transfer from the inductor to workpiece areas. These interconnections strongly depend on the frequency of the electromagnetic field.

Regarding these points, in practice there is a need of a lot of pre-experiments for proper adjustment of a set-up for induction hardening of a newly designed component or when using a different material. That is why this technology is mainly focused to serial productions as a part of a process chain. The planning of the induction hardening process based upon reliable prediction of the outcome is therefore necessary for enhancing operating efficiency and economic viability of small series. Because the physical principles of induction hardening are well known, simulation of induction surface hardening started early. Predictions of hardening profiles were estimated by calculating the energy input and temperature in-depth profiles at simple sample geometries (e.g. [9]). With the improvement of computer technology and the use of finite-element methods the number of successful simulations increased rapidly. For rotation symmetrical samples it was then possible to calculate hardness and surface hardening depth by commercial FE-software. By using sufficient materials parameters good agreement with experimental hardness and surface hardening depth are achieved (e.g. [15]). Nevertheless, three dimensional simulation is still challenging and time consumptive (e.g. [27, 7]).

New requirements for simulation appeared when an electrical concept was developed for connecting power generators which deliver frequencies that differ by approximately a factor of ten to one inductor coil [16]. Thus, eddy currents with different frequency concentrate in separate sample areas. By reducing the heating time and controlling the powers those areas can be heated simultaneously to similar temperature. With this technique it is possible to optimize the thickness of the surface hardening zone to follow a given contour, e.g. of a small gear [2]. A uniformly contour hardened gear with high compressive stresses at the surface is expected to show best results under service conditions.

Finite-element simulation of this multi-frequency technique means that besides the calculation of the thermal field in the three-dimensional sample the electromagnetic field must be calculated at least for two frequencies.

Simulations in 3D using the multi-frequency approach were done by Wrona, [26]. There, the system is solved in the frequency domain using commercial finite element software. Since the software does not support the use of multiple frequencies directly, the different frequency powers are computed stepwise and separately at different time steps on a fixed grid. The stepwise calculation results in an oscillatory behaviour of the temperature, which is not desirable and the consideration of the equations in the frequency domain allows only the use of a constant magnetic permeability. The complete process of multifrequency induction hardening including the quenching stage and the computation of internal stresses is considered in [23]. The computations are carried out in 2D for radial symmetric parts such as shafts. An experimental validation shows good agreement with computational results in the case of multifrequency induction hardening, but only for radial symmetric workpieces. 3D simulations for multifrequency induction hardening of gears are considered in [22]. The magnetic saturation behaviour is taken into account by an iteration procedure, which results in a high increase of computational time.

The aim of this work is the modelling and the simulation of multi-frequency induction hardening in 3D taking into account the phase transition to austenite, quenching by a shower and phase development during quenching. Furthermore, mechanical effects like the residual stress distribution and the distortion caused by phase changes are results of the simulation. This paper covers the full process of induction hardening, including the heating and the quenching stage. The simulations are performed for the case of discs and spur-gears, the results are validated experimentally by simultaneous two-frequency induction hardening. Spur-gears with module 2 and discs with different diameters were hardened. The samples were manufactured from the steel AISI 4140, in hardened and tempered condition, with a tensile strength of about $1100\mathrm{MPa}$. Temperature dependent materials properties and the TTT diagrams of a steel AISI 4140 are implemented in the theoretical models. First results on finite element computations of mechanical strains and stresses can be found in [18].

The paper is organized as follows. In Sec. 2, the equations describing the electromagnetic phenomena, the heat conduction effects, the transformation kinetics and the development of residual stresses are derived.

Sec. 3 is devoted to the numerical simulation of the induction hardening process. The finite element method to solve the system of partial differential equations is introduced. The different aspects arising from nonlinearities, different time scales and other physical properties of the process, which need to be considered in the simulation, are addressed.

Numerical simulations for disc and gear geometries are presented in Sec. 4. The results are compared to experiments. In Sec. 5 we summarize the paper by concluding remarks.

2. THE MODEL

2.1. **Overview.** In order to simulate the complete process of inductive heating and quenching, we need to consider the model components corresponding to the electromagnetic field, the temperature evolution, the steel phase transformations, as well as the mechanical deformations and stresses. The diagram in Figure 1 depicts the interrelations among these physical model components. Given initial conditions at time $t = t_0$ for all model components, we split the complete process of induction hardening occurring during the time interval $(t_0, t_{end}]$ in three main stages, namely:

1 The **heating stage**, at which an alternating current flows through the inductor and generates an alternating magnetic field. This magnetic field induces a voltage and generates eddy currents

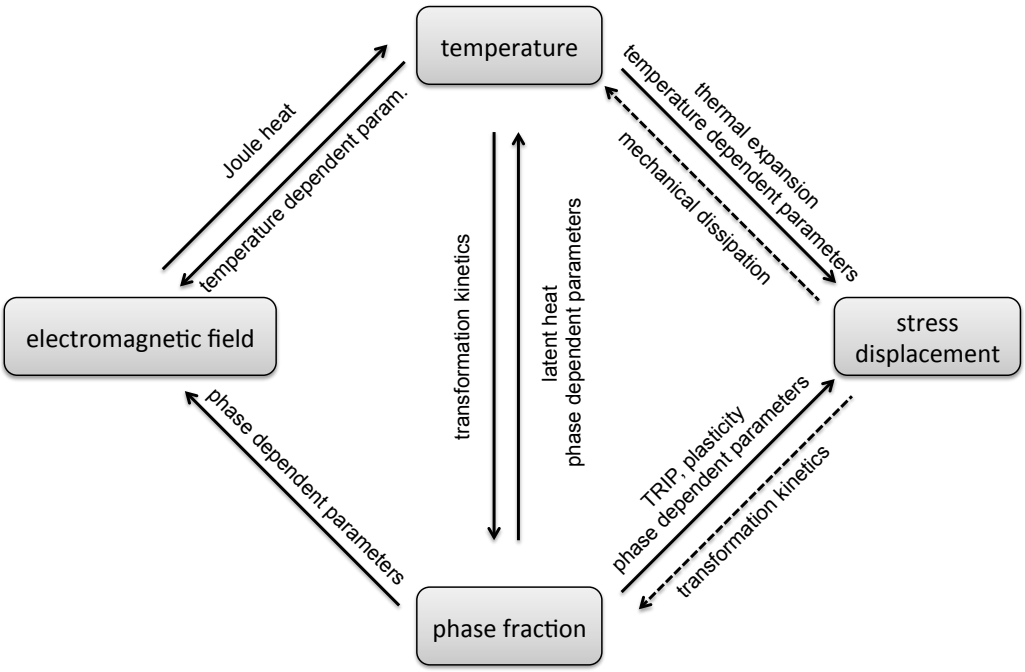

FIGURE 1. Schematic representation of the model

in the workpiece. Due to resistive losses heat is generated directly in the workpiece. This is the first stage of the process, covering a time interval $(t_0, t_1]$.

2 The **down-time stage**, at which the inductive hardening machine changes the piece from the inductor position to the quenching position. This stage corresponds to an unavoidable technical step at which neither the inductor nor the quenching devices are active. We denote the corresponding time interval as $(t_1, t_2]$.

3 The **quenching stage**, at which the component's temperature is strongly decreased using a polymeric quenchant. This stage starts when the quenching device is activated and ends when the component has reached an (almost) homogeneous room temperature. We denote the corresponding interval $(t_2, t_{end}]$

The thermal source is generated by the Joule effect during the heating stage, which is modelled here using Maxwell's equations for the time interval $(t_0, t_1]$. The temperature evolution must be considered for the complete process, having an active heat source only at the beginning and different boundary conditions at the different stages. The phase transformations from the original phase mixture into austenite and its later transition into mainly martensite are also modelled for the heating and quenching stages, respectively. Finally, the mechanical equations to model deformations and stresses are considered for the complete interval $(t_0, t_{end}]$.

The complete model consists of a coupled system of ordinary differential equations for the vector of phases $\boldsymbol{z}$ together with a system of partial differential equations for the temperature θ, the magnetic field $\boldsymbol{H}$ in terms of the magnetic vector potential $\boldsymbol{A}$ and the mechanical deformation, strain and stresses $(\boldsymbol{u}, \varepsilon, \sigma)$. The model for the magnetic field must be resolved in the domain D, which includes the subdomains corresponding to the inductor Ω, the workpiece Σ, and the surrounding air $D \setminus (\Omega \cup \Sigma)$ (cf. Figure 2). The following sections describe each of these sub-modells in detail, together with remarks on the coupling elements (arrows in Figure 1).

2.2. **Maxwell's equations.** The electromagnetic effects are described by Maxwell's equations that are presented in their differential form, [12]. They consist of a system of partial differential equations connecting the magnetic field $\boldsymbol{H}$, the magnetic induction $\boldsymbol{B}$, the electric field $\boldsymbol{E}$ and the electric

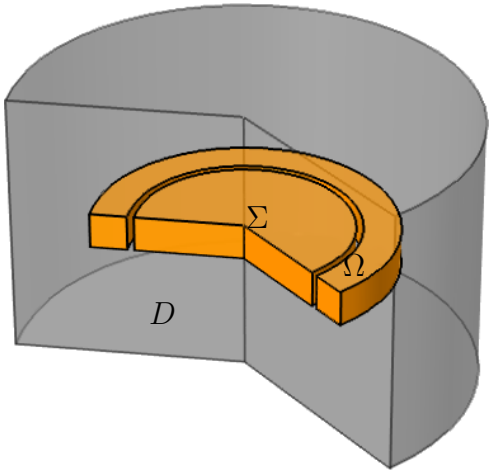

FIGURE 2. Domain D consisting of the inductor Ω, the workpiece Σ and the surrounding air

displacement field $\boldsymbol{D}$

$$\begin{aligned} \operatorname{curl} \boldsymbol{E} &= -\frac{\partial \boldsymbol{B}}{\partial t} \\ \operatorname{div} \boldsymbol{B} &= 0 \\ \operatorname{curl} \boldsymbol{H} &= \boldsymbol{J} + \frac{\partial \boldsymbol{D}}{\partial t} \\ \operatorname{div} \boldsymbol{D} &= \rho. \end{aligned} \tag{1}$$

The quantities on the right hand side are the current density $\boldsymbol{J}$ and the charge density ρ. Maxwell's equations are completed by constitutive laws

$$\boldsymbol{D} = \epsilon \boldsymbol{E} \quad \text{and} \quad \boldsymbol{B} = \mu \boldsymbol{H}, \tag{2}$$

with material dependent parameters μ and ϵ, the magnetic permeability and the electrical permittivity. The current density and the electric field are related by Fourier's law

$$\boldsymbol{J} = \gamma \boldsymbol{E}, \tag{3}$$

where γ denotes the electrical conductivity. The conservation of charge demands that the following compatibility condition holds. Taking the divergence of the third equation in (1) yields

$$\operatorname{div} \boldsymbol{J} + \dot{\rho} = 0. \tag{4}$$

Here and in the sequel $\dot{f}$ denotes the partial derivative with respect to time.

2.3. **Magnetic vector- and electric scalar potential.** To reduce the system consisting of four partial differential equations plus material laws, the vector potential formulation of Maxwell's equations is derived based on Helmholtz decomposition. From $\operatorname{div} \boldsymbol{B} = 0$ we have the existence of the magnetic vector potential $\boldsymbol{A}$ such that

$$\boldsymbol{B} = \operatorname{curl} \boldsymbol{A}. \tag{5}$$

Using (1), there holds

$$\operatorname{curl} \left(\boldsymbol{E} + \dot{\boldsymbol{A}} \right) = 0.$$

As a consequence, we have the existence of the electric scalar potential ϕ such that

$$\boldsymbol{E} = -\nabla \phi - \dot{\boldsymbol{A}}. \tag{6}$$

The magnetic vector potential $\boldsymbol{A}$ is not unique, a gauging condition must be introduced to ensure uniqueness. For induction phenomena, usually the Coulomb-gauging is used

$$\operatorname{div} \boldsymbol{A} = 0. \tag{7}$$

A typical assumption for the modelling of induction phenomena is that the term $\partial \boldsymbol{D}/\partial t$ is small compared to the current density $\boldsymbol{J}$ and can be neglected. The electric field and the current density are linked by Fourier's law (3). The total current density is given by

$$\boldsymbol{J} = -\gamma \dot{\boldsymbol{A}} - \gamma \nabla \phi \tag{8}$$

with $\gamma = 0$ in nonconducting regions. Introducing this relation into (1) yields together with the compatibility condition (4) and the gauging condition (7) the vector potential formulation of Maxwell's equations

$$\begin{aligned} \gamma \dot{\boldsymbol{A}} + \operatorname{curl} \mu^{-1} \operatorname{curl} \boldsymbol{A} + \gamma \nabla \phi = 0 \quad &\text{on} \quad D \times (t_0, t_1] \\ -\operatorname{div} \gamma \nabla \phi = 0 \quad &\text{on} \quad \Omega \times (t_0, t_1]. \end{aligned} \tag{9}$$

Please note that the inductor Ω is the only region with a prescribed source current or source voltage. Therefore, the electric scalar potential vanishes everywhere except for the domain Ω.

In general, Maxwell's equations are defined on an infinite domain. Since the magnetic field decreases to zero with exponential decay in the absence of electric currents, the magnetic vector potential $\boldsymbol{A}$ is set to zero sufficiently far away from the region of interest, i. e. the workpiece and the inductor. Therefore, the surrounding air has to be considered and the boundary condition

$$\boldsymbol{A} \times \boldsymbol{n} = 0 \quad \text{on} \quad \partial D \tag{10}$$

is imposed, where $\boldsymbol{n}$ denotes the outward unit vector on ∂D. For the electric scalar potential there holds

$$\gamma \nabla \phi \cdot \boldsymbol{n} = 0 \quad \text{on} \quad \partial \Omega. \tag{11}$$

The normal derivative $\gamma \nabla \phi \cdot \boldsymbol{n}$ represents the current. Therefore, the condition above corresponds to the fact that there is no current flowing perpendicular to the surface of the inductor.

A prescribed current or voltage source is realized by an interface condition on a cross section area of the inductor denoted by Γ_Ω. The electric current through Γ_Ω is always continuous. The voltage is defined as a potential difference between the connection pins. In our model this is realized by a jump condition for the potential ϕ, i. e.

$$[\![\sigma \nabla \phi]\!] \cdot \boldsymbol{n} = 0 \quad \text{and} \quad [\![\phi]\!] = u(t) \quad \text{on} \quad \Gamma_\Omega, \tag{12}$$

where $[\![\cdot]\!]$ denotes the jump of a quantity across Γ_Ω and $u(t)$ denotes the voltage, see e. g. [17].

2.4. **Characterization of electric sources.** In order to characterize the electric sources in terms of a given voltage or an electric current in the inductor we introduce the source current density as

$$\boldsymbol{J}_{\text{src}} = -\gamma \nabla \phi, \tag{13}$$

that satisfies $\operatorname{div} \boldsymbol{J}_{\text{src}} = 0$. The total current density is then given by $\boldsymbol{J} = -\gamma \dot{\boldsymbol{A}} + \boldsymbol{J}_{\text{src}}$.

In the case of an radial symmetric inductor Ω as e. g. in Figure 2 it is possible to obtain an analytic expression for the electric scalar potential ϕ. We obtain the following expression for the source current density

$$\boldsymbol{J}_{\text{src}}(x,t) = \gamma \frac{u(t)}{2\pi} \boldsymbol{J}_0(x), \tag{14}$$

where $u(t)$ denotes the time dependent voltage in the coil and $\boldsymbol{J}_0$ denoting a geometric form function

$$\boldsymbol{J}_0(x) = \begin{pmatrix} \frac{-y}{x^2+y^2} \\ \frac{x}{x^2+y^2} \\ 0 \end{pmatrix} \quad \text{on} \quad \Omega \tag{15}$$

and equal to zero on $D\backslash\Omega$.

In technical applications, usually the current is controlled. Therefore, we also consider the case of a prescribed inductor current $i(t)$. The current through a cross section A of a conductor is determined as the integral of the current density in normal direction, i. e.

$$i(t) = \int_{\Gamma_\Omega} \boldsymbol{J} \cdot \boldsymbol{n} \, \mathrm{d}a = \int_{\Gamma_\Omega} \gamma \nabla \phi \cdot \boldsymbol{n} \, \mathrm{d}a. \tag{16}$$

Using this equation, we obtain

$$\boldsymbol{J}_{\text{src}}(x,t) = i(t) \frac{\log(r_i/r_a)}{h} \boldsymbol{J}_0(x) \tag{17}$$

with $\boldsymbol{J}_0(x)$ given by (15) and r_i, r_a and h denoting the inner radius, the outer radius and the height of the inductor with rectangular cross section. In the case of multifrequency induction hardening with a prescribed inductor current, the current density $\boldsymbol{J}$ consists of the superimposed medium and high frequency parts of the source current. Assume for simplicity a harmonic source current, then

$$\boldsymbol{J}(x,t) = \left(p_{\text{MF}}(t) I_{\text{MF}} \cos(2\pi f_{\text{MF}} t) + p_{\text{HF}}(t) I_{\text{HF}} \cos(2\pi f_{\text{HF}} t)\right) \frac{\log(r_i/r_a)}{h} \boldsymbol{J}_0(x) \tag{18}$$

in the inductor, where $I_{\text{MF/HF}}$ denote the maximum amplitudes of the MF and HF current. By $p_{\text{MF/HF}}(t) \in [0,1]$ we denote a relative fraction of the medium and high frequency current that corresponds to the relative power and is used as a control parameter for the induction hardening machine. In general, the inductor current is periodic but not necessarily harmonic. We account for this fact by considering the vector potential equation in the time domain instead of the usually used harmonic approach, which is limited to harmonic excitations.

2.5. **Phase transitions.** With regard to phases, the main interest during heat treating of steel components is to create a martensite phase in the areas of interest. This occurs at a crystallographic level during the quenching stage when the conditions of fast cooling rate and the activation temperature has been reached. From experimental experience, it is well known that the main effect of quenching is the transformation of the austenite (generated during the heating stage) into martensite. However, the formation of other phases can also occur, in locations where slower cooling evolutions are reached.

To formulate a model for phase transitions we use here the variables z_1, z_2, z_3, z_4 to denote the phase fractions of austenite, ferrite/pearlite, bainite and martensite, respectively. In addition, we introduce a variable z_0 denoting the initial state of the steel, which consists of a priori unknown amounts of ferrite, martensite, pearlite and/or bainite. The phase fractions sum up to one, e. g. $\sum_{i=0}^{4} z_i = 1$.

During the heating stage, the only phase transition that occurs is the formation of austenite, z_1, from the initial phase mixture z_0. During the subsequent quenching process, the phases ferrite, martensite, bainite and pearlite might build from the transformed austenite.

For the heating stage, the phase evolution of austenite can be described along the ideas given in [10]. In the quenching process, the austenite that formed during the heating stage, transforms into ferrite, pearlite, bainite or martensite, where the rate laws describing this have been presented in [18]. In summary, we model the phases' evolution through the following system of DAEs (differential algebraic

equations):

$$\dot{z}_1 = \frac{(z_1)^r}{\tau(\theta)}[z_{1,\mathsf{eq}}(\theta) - z_1]_+, \qquad t \in [t_0, t_1] \tag{19}$$

$$\dot{z}_2 = -a_2 b_2^{1/a_2}(z_1(t_1) - z_2)\left(\ln\left(1 - \frac{z_2}{z_1(t_1)}\right)\right)^{1-\frac{1}{a_2}}, \qquad t \in [t_1, t_{end}] \tag{20}$$

$$\dot{z}^3 = -a_3 b_3^{1/a_3}(z_1(t_1) - z_2 - z_3)\left(\ln\left(1 - \frac{z_3}{z_1(t_1) - z_2}\right)\right)^{1-\frac{1}{a_3}} - \frac{z_3 \dot{z}_2}{z_1(t_1) - z_2}, \qquad t \in [t_1, t_{end}] \tag{21}$$

$$z_4 = (z_1(t_1) - z_2 - z_3)\left[1 - \left[\frac{\theta - \theta_{end,z_4}}{\theta_{start,z_4} - \theta_{end,z_4}}\right]^n_+\right]_+, \qquad t \in [t_1, t_{end}] \tag{22}$$

with initial values

$$z_1(t_0) = 0 \quad \text{and} \quad z_2(t_1) = z_3(t_1) = z_4(t_1) = 0, \tag{23}$$

where $a_i,\ b_i$ are temperature dependent material parameters and $[\,\cdot\,]_+$ denotes the positive part. Each equation is further activated or deactivated through conditions of the form

$$\dot{z}^i \neq 0 \ \Leftrightarrow\ \theta_{end,z_i} \leq \theta \leq \theta_{start,z_i}, \tag{24}$$

where the activation temperatures θ_{start,z_i} and θ_{end,z_i} can be obtained from the corresponding material TTT diagram. The generation of austenite (19) acts during the heating, the transition to phases $z_2, \ldots, z_4$ during the cooling. For simplicity, we will summarize the set of laws (19)-(22) later on as

$$\dot{\boldsymbol{z}} = f(\boldsymbol{z}, \theta, t).$$

2.6. **Balance of momentum.** During the heating, the down-time, and the quenching stages, the temperature evolution given by equation (41) must be considered together with the corresponding balance of momentum for the mechanical effects. For this, we assume small deformations and follow the ideas used for the quenching stage in [18]. For a more detailed description, we refer to [18] and the references therein.

The balance of momentum without inertial term for the stress σ is used as

$$-\operatorname{div}\sigma = 0. \tag{25}$$

We assume an additive decomposition of the strain into a purely elastic, a thermal, and a third part which stems from a contribution of transformation induced plasticity (TRIP), see [18] for details,

$$\varepsilon(\boldsymbol{u}) = \varepsilon^{\mathsf{el}} + \varepsilon^{\mathsf{th}} + \varepsilon^{\mathsf{trip}}.$$

With this assumption and making use of Hooke's law we can pose the linear relation between stress and the elastic strain as

$$\sigma = C : (\varepsilon(\boldsymbol{u}) - \varepsilon^{\mathsf{th}} - \varepsilon^{\mathsf{trip}}), \tag{26}$$

where $\boldsymbol{u}$ denotes the deformation vector, $\varepsilon(\boldsymbol{u})$ is the total strain

$$\varepsilon(\boldsymbol{u}) = \frac{1}{2}(\nabla \boldsymbol{u} + \nabla \boldsymbol{u}^T), \tag{27}$$

and $\varepsilon^{\mathsf{el}}$, $\varepsilon^{\mathsf{th}}$, $\varepsilon^{\mathsf{trip}}$ are the elastic, thermal and TRIP strains, respectively. C denotes the linear stiffness tensor, which is in general a fourth-order symmetric tensor.

The term ε^{th} corresponds to the mechanical strain resulting from a temperature change in the material. This can be modelled with the density changes as

$$\varepsilon^{\text{th}} = \left(\left(\frac{\overline{\rho}}{\rho(\theta, \boldsymbol{z})} \right)^{\frac{1}{3}} - 1 \right) I. \tag{28}$$

where $\overline{\rho}$ stands for the homogenous density of the initial phase configuration $z_0(t_0)$ at reference temperature θ_{ref}. We propose a mixture ansatz for the density as

$$\rho(\theta, \boldsymbol{z}) = \sum_{i=0}^{4} z_i \rho_i(\theta) \tag{29}$$

with $\rho_i(\theta)$ the homogenous temperature-dependent density of the phase z_i at temperature θ. Using the approach that the thermal part ε^{th} can be subsequently decomposed in an isothermal phase transition effect at reference temperature θ_{ref} and a thermal expansive part without phase transitions, then we obtain (cf. [18])

$$\varepsilon^{\text{th}} \approx -\frac{1}{3} \sum_{i=0}^{4} z_i \left(\frac{\rho_i(\theta_{ref})}{\overline{\rho}} - 1 \right) I + \sum_{i=0}^{4} z_i \alpha^i(\theta)(\theta - \theta_{ref}) I, \tag{30}$$

where $\alpha^i(\theta)$ stands for the linear thermal expansion coefficient of the phase z_i. Moreover we obtain the density $\rho_i(\theta)$ to be expressed as

$$\rho_i(\theta) \approx \rho_i(\theta_{ref}) \left(1 + \alpha^i(\theta)(\theta - \theta_{ref})\right)^{-3}. \tag{31}$$

Following [18], we use a model for the transformation induced plasticity (TRIP) during the quenching stage. The basis of this model is the Franitza-Mitter-Leblond proposal (cf. [18], [6], [5], [14] and [24]), in which the multi-phase formation in the interval $t \in (t_1, t_{end}]$ reads

$$\dot{\varepsilon}^{\text{trip}}(t) = \frac{3}{2} \sigma^* \sum_{i=2}^{4} K_i \left(\theta(t), z_i(\theta(t), t)\right) \left. \frac{\mathrm{d}\phi_i(x)}{\mathrm{d}x} \right|_{z_i(\theta(t),t)} \dot{z}^i(\theta(t), t), \tag{32}$$

where σ^* is the stress deviator, $K_i \in C(\mathbb{R} \times [0,1])$ denote the Greenwood-Johnson parameters for each phase and $\phi_i \in C[0,1] \cap C^1(0,1)$ is the monotone saturation function with $\phi_i(0) = 0$, $\phi_i(1) = 1$. We also assume volume conservation for the inelastic TRIP deformation, i. e. we enforce $\text{tr}(\varepsilon^{trip}) = 0$ and use the initial condition $\varepsilon^{trip}(t = 0) = 0$.

The existent symmetries in the stiffness tensor C for isotropic materials together with the equations above allow for a simplification of the stress expression (26) into

$$\sigma = \lambda \operatorname{div} \boldsymbol{u}\, I + 2\mu\varepsilon(\boldsymbol{u}) - 3\kappa\varepsilon^{\text{th}} - 2\mu\varepsilon^{\text{trip}}. \tag{33}$$

where λ and μ denote the Lamé coefficients and $\kappa = \lambda + \frac{2}{3}\mu$ is the compression modulus. In general, these parameters are (at least) temperature dependent and can be obtained from material measurements.

2.7. **Energy balance.** In order to determine the temperature distribution in the workpiece Σ we consider the balance of energy and the balance of entropy. The temperature distribution in the surrounding air and in the induction coil is not considered. In practical applications, the inductor is cooled. Simulating the cooling process is a complicated task and out of scope of this article.

The balance of internal energy e and the entropy s are given by the following equations

$$\left.\begin{aligned} \overline{\rho}\dot{e} + \operatorname{div} \boldsymbol{q} &= h + \sigma : \dot{\varepsilon} \\ \overline{\rho}\dot{s} + \operatorname{div} \boldsymbol{\phi} &= \zeta \end{aligned}\right\} \quad \text{in} \quad \Sigma \times (t_0, t_{end}], \tag{34}$$

where $\overline{\rho}$ denotes the constant density of the reference configuration, $\boldsymbol{q}$ the heat flux, h the heat source, $\boldsymbol{\phi}$ the entropy flux and ζ the non negative entropy production. The inequality $\zeta \geq 0$ represents the second law of thermodynamics and is used to derive constitutive relations. For ordinary thermoelastic bodies, the entropy flux is defined as $\boldsymbol{\phi} = \boldsymbol{q}/\theta$. For evaluating the second law of thermodynamics, we introduce the free energy $\psi = e - \theta s$. We compute the time derivative $\dot{\psi} = \dot{e} - s\dot{\theta} - \theta\dot{s}$ and introduce the entropy and the energy balance. This yields the expression

$$\begin{aligned} \theta\zeta &= \overline{\rho}\dot{e} - \overline{\rho}s\dot{\theta} - \overline{\rho}\dot{\psi} + \theta \operatorname{div}\frac{\boldsymbol{q}}{\theta} \\ &= h + \sigma : \dot{\varepsilon} - \overline{\rho}s\dot{\theta} - \overline{\rho}\dot{\psi} - \frac{\boldsymbol{q}}{\theta}\nabla\theta. \end{aligned} \tag{35}$$

It is assumed that the free energy density can be expressed by a constitutive function $\psi = \psi(\theta, \boldsymbol{z}, \varepsilon^{\mathsf{el}})$. Introducing the time derivative

$$\dot{\psi} = \frac{\partial\psi}{\partial\theta}\dot{\theta} + \sum_i \frac{\partial\psi}{\partial z_i}\dot{z}_i + \frac{\partial\psi}{\partial\varepsilon^{\mathsf{el}}}\dot{\varepsilon}^{\mathsf{el}}$$

into the entropy balance (35) yields after reordering of the terms

$$\theta\zeta = h - \left(\overline{\rho}s + \overline{\rho}\frac{\partial\psi}{\partial\theta}\right)\dot{\theta} - \sum_i \overline{\rho}\frac{\partial\psi}{\partial z_i}\dot{z}_i + \left(\sigma - \overline{\rho}\frac{\partial\psi}{\partial\varepsilon}\right) : \dot{\varepsilon} - \frac{\boldsymbol{q}}{\theta}\nabla\theta \geq 0. \tag{36}$$

Since the inequality above has to hold for all solutions of the field equations, the terms in front of the time derivatives have to vanish to comply with the second law of thermodynamics. By the usual argumentation, we obtain the following relations. The heat flux is given by Fourier's law,

$$\boldsymbol{q} = -k\nabla\theta. \tag{37}$$

The heat source itself is given by the Joule heat $h = \boldsymbol{J}\cdot\boldsymbol{E} = \gamma\left|\dot{\boldsymbol{A}}\right|^2$ and is a non negative quantity. Furthermore, we derive the relations

$$s = -\frac{\partial\psi}{\partial\theta}, \quad \sigma = \overline{\rho}\frac{\partial\psi}{\partial\varepsilon^{\mathsf{el}}} \tag{38}$$

and we assume that the phase fractions can formally be expressed by the free energy according to $\dot{z}_i = -\Xi_i\partial\psi/\partial z_i$ with positive constants Ξ_i.

In order to derive an expression for the balance of the internal energy we consider

$$\begin{aligned} \dot{s} &= -\frac{\partial^2\psi}{\partial t\partial\theta} = -\frac{\partial}{\partial\theta}\left(\frac{\partial\psi}{\partial\theta}\dot{\theta} + \sum_i \frac{\partial\psi}{\partial z_i}\dot{z}_i + \frac{\partial\psi}{\partial\varepsilon^{\mathsf{el}}} : \dot{\varepsilon}^{\mathsf{el}}\right) \\ &= \frac{\partial s}{\partial\theta}\dot{\theta} + \sum_i \frac{\partial s}{\partial z_i}\dot{z}_i - \frac{1}{\overline{\rho}}\frac{\partial\sigma}{\partial\theta} : \dot{\varepsilon}^{\mathsf{el}}. \end{aligned}$$

For the internal energy holds the relation $e = \psi + \theta s$. Consequently, the time derivative is given by $\dot{e} = \dot{\psi} + s\dot{\theta} + \theta\dot{s}$. Combining the expressions above, we obtain for the internal energy

$$\begin{aligned} \dot{e} &= \frac{\partial\psi}{\partial\theta}\dot{\theta} + \sum_i \frac{\partial\psi}{\partial z_i}\dot{z}_i + \frac{\partial\psi}{\partial\varepsilon^{\mathsf{el}}} : \dot{\varepsilon}^{\mathsf{el}} + s\dot{\theta} + \theta\dot{s} \\ &= \theta\frac{\partial s}{\partial\theta}\dot{\theta} + \sum_i \left(\frac{\partial\psi}{\partial z_i} + \theta\frac{\partial s}{\partial z_i}\right)\dot{z}_i + \left(\frac{1}{\overline{\rho}}\sigma - \theta\frac{\partial\sigma}{\partial\theta}\right) : \dot{\varepsilon}^{\mathsf{el}} \\ &= \theta\frac{\partial s}{\partial\theta}\dot{\theta} + \sum_i \frac{\partial e}{\partial z_i}\dot{z}_i + \left(\frac{1}{\overline{\rho}}\sigma - \theta\frac{\partial\sigma}{\partial\theta}\right) : \dot{\varepsilon}^{\mathsf{el}}. \end{aligned} \tag{39}$$

We define the specific heat at constant deformation c_ε and the latent heat for the phase transformation from the initial phase mixture z_0 to austenite z_1 by

$$c_\varepsilon = \theta \frac{\partial s}{\partial \theta} \quad \text{and} \quad L^{01} = \frac{\partial e}{\partial z_0} - \frac{\partial e}{\partial z_1}. \tag{40}$$

Analogously, we define the latent heat coefficients for the phase transformation from austenite to ferrite, pearlite, bainite and martensite by

$$L^{1i} = \frac{\partial e}{\partial z_1} - \frac{\partial e}{\partial z_i}, \quad i = 2, \dots, 4.$$

Introducing these quantities into the energy balance (34) and making use of the fact that $\sum_{i=0}^{4} z_i = 1$ such that $\sum_{i=0}^{4} \partial z_i / \partial t = 0$ we eliminate z_1 and obtain

$$\begin{aligned} \overline{\rho} c_\varepsilon \dot{\theta} - \operatorname{div} k \nabla \theta = \gamma \left| \dot{\boldsymbol{A}} \right|^2 - \overline{\rho} L^{01} \dot{z}_0 + \overline{\rho} \sum_{i=2}^{4} L^{1i} \dot{z}_i \\ + \sigma : (\dot{\varepsilon}^{\text{th}} + \dot{\varepsilon}^{\text{trip}}) + \overline{\rho} \theta \frac{\partial \sigma}{\partial \theta} : \dot{\varepsilon}^{\text{el}} \quad \text{in} \quad \Sigma \times (t_0, t_{end}]. \end{aligned} \tag{41}$$

The term for the mechanical dissipation in the heat equation is approached as the sum of the thermal and the TRIP effects (cf. [10], [18]), the term $\partial \sigma / \partial \theta$ is assumed to be small and is neglected. As presented in [18], the thermal part reads

$$\begin{aligned} \sigma : \dot{\varepsilon}^{\text{th}} = \Bigg[\left(\sum_{i=0}^{4} z_i \alpha^i + (\theta - \theta_{ref}) \sum_{i=0}^{4} z_i \alpha^i \right) \dot{\theta} + (\theta - \theta_{ref}) \sum_{i=0}^{4} \dot{z}^i \alpha^i \\ - \frac{1}{3} \sum_{i=0}^{4} \dot{z}^i \left(\frac{\rho_i(\theta_{ref})}{\overline{\rho}} - 1 \right) \Bigg] \operatorname{tr} \sigma \end{aligned} \tag{42}$$

and the TRIP effect

$$\sigma : \dot{\varepsilon}^{\text{trip}} = \frac{3}{2} |\sigma^*|^2 \sum_{i=2}^{4} K_i(\theta(t), z_i) \left. \frac{\mathrm{d}\phi_i(x)}{\mathrm{d}x} \right|_{z_i(\theta(t),t)} \dot{z}^i(\theta(t), t). \tag{43}$$

3. Numerical discretization

Assuming that the workpiece has symmetric properties, both equatorial and rotational, the computational domain D and consequently Σ can be reduced to a segment with certain angle by slicing it along the middle plane towards the center of the workpiece and subsequent cutting in suitable longitudinal direction. Then the numerical computation can be reduced by considering the corresponding boundary conditions on the middle plane denoted by Γ_s and sectional symmetry planes Γ_v (cf. [18]).

Introducing this domain reduction technic from symmetry reasons and summarizing Sec. 2, the induction hardening problem consists of finding functions $\boldsymbol{A}(x,t), \theta(x,t), z(x,t)$ and $\boldsymbol{u}(x,t)$ that satisfy the following system of partial and ordinary differential equations

$$\gamma \dot{\boldsymbol{A}} + \operatorname{curl} \mu^{-1} \operatorname{curl} \boldsymbol{A} = \boldsymbol{J}_{\text{src}} \qquad \text{in } D \times (t_0, t_1] \tag{44}$$

$$\overline{\rho} c_\varepsilon \dot{\theta} - \operatorname{div} k \nabla \theta = \hat{f} \qquad \text{in } \Sigma \times (t_0, t_{end}] \tag{45}$$

$$-\operatorname{div} \sigma = 0 \qquad \text{in } \Sigma \times (t_0, t_{end}] \tag{46}$$

$$\dot{\varepsilon}^{\text{trip}} = f^{\text{trip}}(\sigma, \theta, \boldsymbol{z}, \dot{\boldsymbol{z}}) \qquad \text{in } \Sigma \times (t_0, t_{end}] \tag{47}$$

$$\dot{\boldsymbol{z}} = f(\boldsymbol{z}, \theta, t) \qquad \text{in } \Sigma \times (t_0, t_{end}] \tag{48}$$

with suitable initial conditions, where $\hat{f} = \gamma \left|\dot{\boldsymbol{A}}\right|^2 + \sigma : (\dot{\varepsilon}^{\text{th}} + \dot{\varepsilon}^{\text{trip}}) - \overline{\rho}\boldsymbol{L} \cdot \dot{\boldsymbol{z}}$ is used as abbreviation for the right hand side and $\boldsymbol{J}_{\text{src}}$ given by (17).

Since the computational domain has been reduced, boundary conditions for the vector potential $\boldsymbol{A}$ need to be defined on the middle and sectional symmetry planes. The source current $\boldsymbol{J}_{\text{src}}$ is defined only in angular direction. Therefore, the tangential components of $\boldsymbol{A}$ vanish on the vertical cutting surfaces Γ_v. On the horizontal symmetry plane Γ_s the magnetic field $\boldsymbol{H} = \mu^{-1} \operatorname{curl} \boldsymbol{A}$ admits only normal components such that all together there holds

$$\boldsymbol{A} \times \boldsymbol{n} = 0 \quad \text{on } \Gamma_v \quad \text{and} \quad \mu^{-1} \operatorname{curl} \boldsymbol{A} \times \boldsymbol{n} = 0 \quad \text{on } \Gamma_s.$$

In order to adapt the boundary conditions of the thermomechanical equations (45) and (46) to the reduced geometry, the workpiece boundary $\partial\Sigma$ is assumed to be dissected into a part τ_p where a pressure $p = (p_1, p_2, p_3)^T$ is applied, a part τ_u which is fixed and a part $\tau_s = \partial\Sigma \cap (\Gamma_s \cup \Gamma_v)$ which serves as the total symmetry plane.

For the heat equation the thermal flow at the symmetry plane is null, which yields the boundary conditions corresponding to (45):

$$\begin{aligned} -k\nabla\theta \cdot \boldsymbol{n}_p &= \eta(\theta - \theta_{ext}), && \text{on } \tau_p \\ -k\nabla\theta \cdot \boldsymbol{n}_u &= 0, && \text{on } \tau_u \\ -k\nabla\theta \cdot \boldsymbol{n}_s &= 0, && \text{on } \tau_s, \end{aligned} \tag{49}$$

where $\boldsymbol{n}_p,\ \boldsymbol{n}_u,\ \boldsymbol{n}_s$ represent the normal on $\tau_p,\ \tau_u$ and τ_s. Regarding the boundary conditions to (46) we use the symmetry property and obtain

$$\sigma\, \boldsymbol{n}_p = p, \text{ on } \tau_p, \tag{50}$$

$$\boldsymbol{u} = 0, \text{ on } \tau_u, \tag{51}$$

$$\boldsymbol{u} \cdot \boldsymbol{n}_s = 0, \text{ on } \tau_s, \tag{52}$$

$$\nabla(\boldsymbol{u} \cdot \boldsymbol{\tau}_s^1) \cdot \boldsymbol{n}_s = 0, \text{ on } \tau_s, \tag{53}$$

$$\nabla(\boldsymbol{u} \cdot \boldsymbol{\tau}_s^2) \cdot \boldsymbol{n}_s = 0, \text{ on } \tau_s, \tag{54}$$

where the tangential vectors $\boldsymbol{\tau}_s^1, \boldsymbol{\tau}_s^2$ are linearly independent and orthogonal to $\boldsymbol{n}_s = (n_s^x, n_s^y, n_s^z)^T$. For simplicity we assume furthermore that $n_s^x + n_s^y + n_s^z \neq 0$. This restriction can be satisfied by selecting suitable orthogonal coordinates.

The induction heating model represents an evolutionary problem. The common approach is to discretize the equations with respect to space and with respect to time separately. At first, the equations are discretized in space by a Galerkin method. This is presented in Section 3.1. As a result one obtains a system of ordinary differential equations. The discretization with respect to time is considered in Section 3.2. Regarding the time discretization, the electromagnetic and the thermomechanical effects admit different time scales. Therefore it is the aim to decouple the system of equations and solve the space discretized equations with different time steps δt and Δt.

3.1. **Discretization in space.** The discretization in space is obtained by the Galerkin method solving the variational formulation corresponding to (44)–(48). It is assumed that for fixed time $t \in (t_0, t_{end})$, the continuous problem possesses a solution $\boldsymbol{A}(t)$ in some space $\mathbb{W}$, $\theta(t)$ in V, $\boldsymbol{u}(t)$ in $\mathbb{X}$ and $z(t)$ in Z. Due to the non-linearities in (44)–(48), a concrete definition for the spaces $\mathbb{W}, V$ and Z is difficult, we refer to [11], where the existence and uniqueness of solutions for a reduced model is investigated.

Considering the vector potential equation, the weak formulation is: Find $\boldsymbol{A}(t) \in \mathbb{W}$ such that

$$\int_D \gamma \dot{\boldsymbol{A}} \cdot \boldsymbol{\psi}\, \mathrm{d}x + \int_D \mu^{-1} \operatorname{curl} \boldsymbol{A} \cdot \operatorname{curl} \boldsymbol{\psi}\, \mathrm{d}x = \int_D \boldsymbol{J}_{\text{src}} \cdot \boldsymbol{\psi}\, \mathrm{d}x \tag{55}$$

for all $\boldsymbol{\psi} \in \mathbb{W}$. The gauging condition $\operatorname{div} \boldsymbol{A} = 0$ is not included in the weak formulation above, it is considered in terms of a regularization of the electrical conductivity in non-conducting regions, i. e. $\gamma = \epsilon > 0$ for $x \in D \setminus (\Omega \cup \Sigma)$.

In order to define the weak formulation of the thermomechanical model, let us introduce the Sobolev space $\mathbb{X}$ whose trace matches the Dirichlet and the symmetry boundary conditions of the displacement $\boldsymbol{u}$ as

$$\mathbb{X} = \{\boldsymbol{v} : \Sigma \to \mathbb{R}^3 \ : \ \boldsymbol{v} \in \mathbb{H}^1(\Sigma) \text{ and } \boldsymbol{v} \cdot \boldsymbol{n}_s|_{\tau_s} = 0, \ \boldsymbol{v}|_{\tau_u} = 0\},$$

where $\mathbb{H}^1(\Sigma)$ denotes the vector valued counterpart to the Sobolev space $H^1(\Sigma)$. Having in mind all boundary conditions (49)-(54) we define the weak formulation of the thermomechanical model:

Find $\theta(t) \in V$ and $\boldsymbol{u}(t) \in \mathbb{X}$ such that

$$\begin{aligned} \int_\Sigma \overline{\rho} c_\varepsilon \dot{\theta}\, \varphi \,\mathrm{d}x + \int_\Sigma k \nabla\theta \cdot \nabla\varphi \,\mathrm{d}x + \int_{\tau_p} \eta\theta\, \varphi \,\mathrm{d}a &= \int_\Sigma \hat{f}\, \varphi \,\mathrm{d}x + \int_{\tau_p} \eta\theta_{ext}\, \varphi \,\mathrm{d}a \\ \int_\Sigma \sigma : \varepsilon(\boldsymbol{\phi}) \,\mathrm{d}x &= \int_{\tau_p} p \cdot \boldsymbol{\phi} \,\mathrm{d}x \end{aligned} \tag{56}$$

for all $\varphi \in V$, $\boldsymbol{\phi} \in \mathbb{X}$ and a. e. in $(t_0, t_{end}]$. The ODE to determine the phase fractions is still considered in its strong form

$$\dot{\boldsymbol{z}} = f(\boldsymbol{z}, \theta, t).$$

As initial conditions, we define

$$\boldsymbol{A}(x, t_0) = \boldsymbol{A}_0(x), \quad \theta(x, t_0) = \theta_0(x), \quad \boldsymbol{u}(x, t_0) = \boldsymbol{u}_0(x), \quad \boldsymbol{z}(x, t_0) = \boldsymbol{z}_0(x). \tag{57}$$

The fundamental approach of the finite element method as a special case of the Galerkin method is to find approximate solutions $\boldsymbol{A}_h(t), \theta_h(t), \boldsymbol{u}(t)$ and $z_h(t)$ in suitable finite dimensional sub-spaces $\mathbb{W}_h, V_h = Z_h$ and $\mathbb{X}_h$ to discretize the magnetic vector potential, the temperature, the displacement and the volume fraction of austenite with respect to space.

Let $\mathcal{T}_h$ be a triangulation of D (resp. the reduced segment) that respects the subdomain Σ. We discretize the heat equation by piecewise linear elements:

$$V_h = \{v \in H^1(\Sigma) \ : \ v|_K \in \mathcal{P}_1(K) \quad \text{for all} \quad K \in \mathcal{T}_h \cap \Sigma\}, \tag{58}$$

and use piecewise polynomial Lagrange finite elements φ_i as a basis, e. g. :

$$V_h = \operatorname{span}\{\varphi_j\}_{j=1,\dots,N}.$$

In general, the space of solutions for the vector potential equation is a subspace of

$$H(\operatorname{curl}, d) := \{\boldsymbol{w} \in L^2(D) \mid \operatorname{curl} \boldsymbol{w} \in L^2(D)\}. \tag{59}$$

Elements $\boldsymbol{w} \in H(\operatorname{curl}, d)$ possess certain continuity properties at material boundaries. These functions are only continuous in tangential direction, in normal direction discontinuities might occur. The finite element discretization of $\mathbb{W} \subset H(\operatorname{curl}, d)$ has to preserve this property. Using piecewise polynomial Lagrange elements as in (58) for each space dimension would reduce the accuracy of the numerical solution. Therefore, we use lowest order Nédélec elements for the discretization of the vector potential equation

$$\mathbb{W}_h = \{\boldsymbol{v} \in \mathbb{W} \ : \ \boldsymbol{v}|_K \in \mathcal{N}_0(K) \quad \text{for all} \quad K \in \mathcal{T}_h\} \tag{60}$$

with $\mathcal{N}_0(K)$ denoting the polynomial space $\mathcal{N}_0(K) = \{\boldsymbol{a} + \boldsymbol{b} \times x \ : \ \boldsymbol{a}, \boldsymbol{b} \in \mathbb{R}^3\}$, [19]. We introduce basis functions $\boldsymbol{\eta}_j$ such that $\mathbb{W}_h = \operatorname{span}\{\boldsymbol{\eta}_j\}_{j=1,\dots,N_E}$.

To identify a basis of $\mathbb{X}_h$ for the discretization of displacements $\boldsymbol{u}$ via equation (46) we use a direct sum:

$$\mathbb{X}_h = U_s \oplus U_r$$

where

$$U_s := \text{span}\left\{ \begin{pmatrix} (n_s^y + n_s^z)\varphi_l \\ -n_s^x\varphi_l \\ -n_s^x\varphi_l \end{pmatrix}, \begin{pmatrix} -n_s^y\varphi_l \\ (n_s^x + n_s^z)\varphi_l \\ -n_s^y\varphi_l \end{pmatrix} \right\}_{l \in N_{\tau_s}}, \tag{61}$$

$$U_r := \text{span}\left\{ \begin{pmatrix} \varphi_s \\ 0 \\ 0 \end{pmatrix}, \begin{pmatrix} 0 \\ \varphi_s \\ 0 \end{pmatrix}, \begin{pmatrix} 0 \\ 0 \\ \varphi_s \end{pmatrix} \right\}_{s \in N_{\tau_p} \cup N_{in}}, \tag{62}$$

N_{τ_s}, N_{τ_p}, N_{in} denote degrees of freedom on τ_s, τ_p and the interior of the reduced workpiece respectively. Then we have

$$\mathbb{X}_h = \text{span}\{\boldsymbol{\phi}_j\}_{j=1,\dots,N_{\tau_s}+N_{\tau_p}+N_{in}}.$$

The vector of phase fractions $\boldsymbol{z}$ is discretized using the finite element interpolation operator $\mathcal{I}_{\mathcal{T}} : Z \to V_h$ such that

$$z_{i,h} = \mathcal{I}_{\mathcal{T}}(z_i) = \sum_{j=1}^{N} z_i^j \varphi_j, \quad i = 0, \dots, 4,$$

where z_i^j are the coefficients of the finite element representation of $z_{i,h}$. Using P1-elements to discretize the phase fractions z_i, the evaluation of the interpolation operator $\mathcal{I}_{\mathcal{T}}$ consists in evaluating the corresponding function at nodes of the mesh. This is also carried out on the right hand side of the ODE such that

$$\dot{\boldsymbol{z}}_h = f_h(\boldsymbol{z}_h, \theta_h, t), \tag{63}$$

where $f_h(\boldsymbol{z}_h, \theta_h, t) = \mathcal{I}_{\mathcal{T}}(f(\boldsymbol{z}, \theta, t))$.

Finally, we obtain a nonlinear system of equations, where underlined quantities denote the vector representing the finite element function, i. e. $\underline{\theta} = \{\theta_i\}_{i=1,\dots,N}$ where $\theta_h = \sum_{i=1}^{N} \theta_i \, \varphi_i$

$$\begin{aligned}
\boldsymbol{M}_\gamma \dot{\underline{A}} + \boldsymbol{K}_\mu \underline{A} &= \hat{J} && \text{for } t \in (t_0, t_1] \\
\boldsymbol{D}_{\rho c} \dot{\underline{\theta}} + \boldsymbol{S}_\kappa \underline{\theta} &= \hat{F} && \text{for } t \in (t_0, t_{end}] \\
\boldsymbol{Q}_{\mu\lambda} \underline{u} &= \hat{H} && \text{for } t \in (t_0, t_{end}] \\
\dot{\underline{\varepsilon}}^{\text{trip}} &= f_h^{\text{trip}}(\sigma, \underline{\theta}, \underline{z}, \dot{\underline{z}}) && \text{for } t \in (t_0, t_{end}] \\
\dot{\underline{z}} &= f_h(\underline{z}, \underline{\theta}, t) && \text{for } t \in (t_0, t_{end}].
\end{aligned} \tag{64}$$

The last equation is formulated for the vector $\underline{z}$ and has to be understood elementwise in the sense of (63).

Furthermore, initial conditions have to be defined for $\underline{A}, \underline{\theta}, \underline{u}$ and $\underline{z}$ that are consistent with (57), e. g.

$$\begin{aligned}
&\boldsymbol{A}_h(x, t_0) = \mathcal{I}_{\mathcal{T}}(A_0(x)), \quad \theta_h(x, t_0) = \mathcal{I}_{\mathcal{T}}(\theta_0(x)), \\
&\boldsymbol{u}_h(x, t_0) = \mathcal{I}_{\mathcal{T}}(\boldsymbol{u}_0(x)), \quad \varepsilon_h^{\text{trip}}(x, t_0) = 0, \quad \boldsymbol{z}_h(x, t_0) = \mathcal{I}_{\mathcal{T}}(\boldsymbol{z}_0(x)).
\end{aligned} \tag{65}$$

Above, we use the matrices

$$
\begin{aligned}
\boldsymbol{M}_\gamma &= M_{\gamma,ij} \qquad \text{with} \quad M_{\gamma,ij} = \int_D \gamma \boldsymbol{\eta}_i \cdot \boldsymbol{\eta}_j \,\mathrm{d}x,\\
\boldsymbol{K}_\mu &= K_{\mu,ij} \qquad \text{with} \quad K_{\mu,ij} = \int_D \mu^{-1} \operatorname{curl} \boldsymbol{\eta}_i \cdot \operatorname{curl} \boldsymbol{\eta}_j \,\mathrm{d}x,\\
\boldsymbol{D}_{\rho c} &= D_{\rho c,ij} \qquad \text{with} \quad D_{\rho c,ij} = \int_\Sigma \overline{\rho} c_\varepsilon \varphi_i \, \varphi_j \,\mathrm{d}x,\\
\boldsymbol{S}_\kappa &= S_{\kappa,ij} \qquad \text{with} \quad S_{\kappa,ij} = \int_\Sigma M \nabla \varphi_i \cdot \nabla \varphi_j \,\mathrm{d}x + \int_{\tau_p} \eta \varphi_i \varphi_j \,\mathrm{d}a,\\
\boldsymbol{Q}_{\mu\lambda} &= Q_{\mu\lambda,ij} \qquad \text{with} \quad Q_{\mu\lambda,ij} = \int_\Sigma (\mu \nabla \boldsymbol{\phi}_i : \nabla \boldsymbol{\phi}_j + (\lambda+\mu) \mathsf{div}\, \boldsymbol{\phi}_i \mathsf{div}\, \boldsymbol{\phi}_j) \,\mathrm{d}x.
\end{aligned}
\tag{66}
$$

The matrix $\boldsymbol{M}_\gamma$ denotes the mass matrix associated to W_h and $\boldsymbol{K}_\mu$ the curl-curl matrix, $\boldsymbol{D}_{\rho c}$ the thermal mass matrix, $\boldsymbol{S}_\kappa$ the thermal diffusion matrix, $\boldsymbol{Q}_{\mu\lambda}$ the stiffness matrix associated to $\boldsymbol{u}$. The right hand side is abbreviated by (nonlinear) vectors $\hat{J}(t) = \hat{J}_j$, $\hat{F}(\underline{\theta}, \underline{A}, \underline{z}) = \hat{F}_j$, and $\hat{H}(\underline{\varepsilon}^{\mathsf{th}}, \underline{\varepsilon}^{\mathsf{trip}}) = \hat{H}_j$ which are given explicitly as

$$
\begin{aligned}
\hat{J}_j &= \int_D \boldsymbol{J}_{\mathsf{src}}(t) \cdot \boldsymbol{\eta}_j \,\mathrm{d}x,\\
\hat{F}_j &= \int_\Sigma \hat{f}(\theta_h, \boldsymbol{A}_h, z_h) \, \varphi_j \,\mathrm{d}x + \theta_{ext} \int_{\tau_p} \eta_h \varphi_j \,\mathrm{d}a,\\
\hat{H}_j &= \int_\Sigma (3\kappa \varepsilon_h^{\mathsf{th}} + 2\mu \varepsilon_h^{\mathsf{trip}}) : \nabla \boldsymbol{\phi}_j \,\mathrm{d}x + \int_{\tau_p} p_h \cdot \boldsymbol{\phi}_j \,\mathrm{d}a.
\end{aligned}
\tag{67}
$$

A more detailed description of the numerical discretization for the induction hardening problem can be found in [18, 21].

The nonlinear system (64) obtained by discretization in space has to be solved by suitable methods. This involves solution strategies to handle the nonlinearities appearing on the right hand side and within the matrices (66), a discretization of the ordinary differential equation in time and of course, solving the resulting system of linear equations by direct or iterative methods.

3.2. **Discretization in time.** If we consider the vector potential equation (44) for a fixed temperature θ, then it represents a parabolic equation that admits a time periodic solution due to the time periodic source term. We solve this equation for some periods using an order two time stepping scheme with time step δt.

The heat equation (45) also represents a parabolic equation with rapidly varying right hand side $\gamma|\dot{\boldsymbol{A}}|^2$. Since heat conduction is supposed to happen on a time scale that is much slower than the oscillating current, the temperature changes at a time scale that is much larger than that of the right hand side which is governed by the frequency of the source current. The usual approach is to approximate the Joule heat term by its average over one period, [4]. Then, we can solve the heat equation together with the quasistatic balance of momentum and the ODE describing the phase transition using time steps $\Delta t \gg \delta t$, where we replace the rapidly varying Joule heat by an averaged Joule heat term that is obtained from the solution of the vector potential equation.

We formulate the algorithm as follows. We consider the time interval (t_0, t_1) and decompose it into M equal time steps t^k with time step size $\Delta t = (t_1 - t_0)/M$ such that

$$
t^k = k\Delta t \quad \text{for} \quad k = 1, \ldots, M.
$$

The ‘large’ time step size Δt results from the typical time scale of the heat conduction.

We obtain time intervals $(t^k, t^{k+1}),\ k = 0, \ldots, M-1$, on which we solve the electromagnetic problem under the assumption that the temperature is constant in time. For this we use a time step $\delta t \ll \Delta t$ that is related to the source term of the vector potential equation. We obtain a decomposition of the intervals (t^k, t^{k+1}) such that

$$t^{k,l} = t^k + l\delta t \quad \text{for} \quad l = 0, 1, \ldots$$

and solve the vector potential equation by a time stepping scheme of order two (e. g. Crank-Nicholson). In general, it is not necessary to solve for $\boldsymbol{A}$ on the whole interval (t^k, t^{k+1}). Since the source term $\boldsymbol{J}_{\text{src}}$ and consequently $\boldsymbol{A}$ is periodic, it is sufficient to solve until a periodic solution is obtained.

The Joule heat, that enters the right hand side of the time stepping scheme of the heat equation is obtained by averaging the term $\gamma|\dot{\boldsymbol{A}}|^2$ over one period,

$$\overline{h} = \frac{\omega}{2\pi} \int_0^{\frac{2\pi}{\omega}} \gamma \left|\dot{\boldsymbol{A}}\right|^2 \, \mathrm{d}t. \tag{68}$$

The averaged Joule heat $\overline{h}$ is still time dependent due to the temperature and phase dependent electrical conductivity $\gamma(\theta, z)$, but it is not highly oscillating any more. Finally, we have decoupled the vector potential equation and the heat equation together with the rate law for the phase fraction. Having determined the Joule heat, the heat equation together with the balance of momentum and the rate laws to determine $\boldsymbol{z}$ can be solved by a suitable time stepping scheme at the discrete times $t^k,\ k = 1, \ldots, M$. For the quenching period on the time interval $(t_1, t_{end}]$ this two step algorithm is not necessary.

The semi-discretized system in space (64) is now solved in time by the afore mentioned algorithm. Since the time derivative of $\boldsymbol{A}$ is used to evaluate the Joule heat, we are interested in its accurate approximation and use a Crank-Nicholson scheme that approximates the time derivative with order two. For the integration of the heat equation, we simply use an implicit Euler method. The resulting systems are highly non-linear, since the right hand side and the material parameters depend non-linearly on the unknown fields. Instead of using Newtons method, we propose a semi-implicit discretization. With this method, only linear terms are evaluated implicitly at time t^{k+1}. Nonlinear terms, especially the material parameters, are evaluated at the old time step t^k. The resulting linear systems are solved by a combination of the direct solver PARDISO and a preconditioned CG method.

3.3. **The non-linear magnetization curve.** In ferromagnetic materials, the magnetic permeability is a nonlinear function. It depends on the temperature θ and the magnetic field $\boldsymbol{H}$, such that $\mu = \mu(\theta, |\boldsymbol{H}|)$.

In order to avoid small time steps to resolve the non-linear permeability during the solution of $\boldsymbol{A}(x,t)$ and to avoid a permanent reassembly of the permittivity matrix $\boldsymbol{K}_\mu$, we introduce an averaging procedure proposed in [4] to linearize the vector potential equation.

In induction heating problems, the focus lies on the efficient computation of the Joule heat. The exact reproduction of the magnetic fields is of minor importance as long as the Joule heat term $\boldsymbol{J} \cdot \boldsymbol{E} = \gamma|\dot{\boldsymbol{A}}|^2$ is approximated with sufficient accuracy. It is assumed, that only a time averaged value of the permeability affects the magnetic field.

After having decoupled the heat- and the vector potential equation as described in Section 3.2 we consider the time interval (t^k, t^{k+1}) and assume the temperature at time t^k is known. Furthermore, we assume, that we have solved Maxwell's equations and a periodic solution to $\boldsymbol{A}$ is known on (t^k, t^{k+1}). Then, the periodic magnetic field intensity is given by $\boldsymbol{H} = \mu^{-1} \operatorname{curl} \boldsymbol{A}$. The exact magnetic permeability is then a periodic function given by

$$\mu(x,t) = \mu(\theta^k(x), |\boldsymbol{H}(x,t)|). \tag{69}$$

We define an averaged magnetic permeability $\overline{\mu}(x)$ as

$$\frac{1}{\overline{\mu}(x)} = \frac{\omega}{2\pi} \int_0^{\frac{2\pi}{\omega}} \frac{1}{\tilde{\mu}(x,t)} \, \mathrm{d}x. \tag{70}$$

Using the inverse of μ for the averaging procedure is proposed in [4]. The permeability $\overline{\mu}(x)$ is now independent of $\boldsymbol{A}$, it only depends on the space coordinate x and has to be computed in every point of the domain. Since $\boldsymbol{A}$ is not a priori known, $\overline{\mu}$ has to be computed iteratively.

The advantage of the averaged permeability is, that $\overline{\mu}$ is fixed for one θ-time step, the vector potential equation is linear. There is no need to reassemble the system matrices $\boldsymbol{K}_\mu$.

The linearization of μ is a common approach. A similar fixed point iteration as described above is introduced in [13]. Though the paper appeared in 1989, the technique is also used in actual publications related to induction hardening, [8, 23]. This approach introduces a fictional linear material with a fictive permeability μ^f. By an iterative procedure, the fictive permeability is computed by energetic considerations. This approach can be easily implemented when considering Maxwell's equations in the frequency domain, since it only involves the magnetic energy $\boldsymbol{H} \cdot \boldsymbol{B}$. Ostrowski [20] introduces an effective permeability μ_{eff}, also by averaging the nonlinear permeability over one period.

3.4. **The skin effect.** Solutions to the vector potential equation admit only tangential continuity. At material interfaces, the normal component of $\boldsymbol{A}$ can be discontinuous and might admit strong singularities. In addition, due to the skin effect, the eddy currents are concentrated in the surface region of the workpiece Σ.

In order to obtain accurate results, the mesh of the finite element discretization has to be fine enough to resolve material interfaces and the surface area of the workpiece. On the other hand one is interested in reducing the computational cost, especially for 3D computations, such that it is desirable to use a coarse mesh in regions that are sufficiently far away from the zone of interest.

Therefore, we create an adaptive grid, that has a high resolution in the surface area of the workpiece and at interfaces, where material properties might change and is coarse in regions where a high accuracy is not necessary.

This requires a posteriori error estimators to get information on the local error of the computed approximative solution to the magnetic vector potential. These error estimators provide an indicator, which mesh cells need to be refined and which cells might be coarsened.

A posteriori error estimators are a well established tool for the effective numerical solution of elliptic boundary value problems. In general, an adaptive algorithm has the following general structure, [25]:

1 Construction of an initial coarse mesh $\mathcal{T}_k$, with $k = 0$.
2 Solve the discrete problem on the triangulation $\mathcal{T}_k$.
3 Compute the a posteriori error indicator on each element $K \in \mathcal{T}_k$.
4 If the estimated error is below some tolerance ϵ then stop. Otherwise select elements $K \in \mathcal{T}_k$ to refine and create a new mesh. Increment k by 1 and go to (ii).

In the adaptive algorithm, we will not consider the discretization errors in time. We only consider the spatial error and derive error estimators that estimate the error for fixed given times t^k. Since the temporal error is not controlled, the time steps to discretize the vector potential equation and the heat equation have to be taken sufficiently small such that the contribution of the temporal error is of similar order as the spatial error.

For finite element approximations using Nédélec elements, fundamental results on a posteriori error estimators were obtained by Beck et al., [1]. We use the error estimator introduced in this article to

generate adaptive grids for the solution of the induction heating problem. Considered is an abstract problem: Find $\boldsymbol{u} \in H(\mathrm{curl}, D)$ such that

$$\mathrm{curl}\,(\chi\,\mathrm{curl}\,\boldsymbol{u}) + \beta\boldsymbol{u} = \boldsymbol{f} \quad \text{in } D, \quad \boldsymbol{u} \times \boldsymbol{n} = 0 \quad \text{on } \partial D$$

where $\chi \in L^\infty(D)$ uniformly bounded away from zero and $\beta \in L^\infty(D)$ with $\beta \geq 0$. An estimate for the error on each element $K \in \mathcal{T}_h$ is obtained by

$$\widehat{\eta}_K^2 = h_T^2 \left\| \frac{1}{\sqrt{\chi}} (\pi_h \boldsymbol{f} - \beta \tilde{\boldsymbol{u}}_h) \right\|^2_{\mathbb{L}^2(K)} + \sum_{F \in \mathcal{F}_K} \frac{h_F}{2} \left(\frac{\beta_{|K}}{\overline{\beta}_F} \left\| \frac{1}{\sqrt{\overline{\beta}_F}} [\![\boldsymbol{n} \cdot \beta \tilde{\boldsymbol{u}}_h]\!]_F \right\|^2_{L^2(F)} + \frac{\chi_{|K}}{\overline{\chi}_F} \left\| \frac{1}{\sqrt{\overline{\chi}_F}} [\![\boldsymbol{n} \times \chi\,\mathrm{curl}\,\tilde{\boldsymbol{u}}_h]\!]_F \right\|^2_{\mathbb{L}^2(F)} \right), \tag{71}$$

where $\tilde{\boldsymbol{u}}_h$ denotes the approximative solution, h_K and h_F the maximal diameter of an element $K \in \mathcal{T}_h$ and a face $F \in \mathcal{F}_K$ with $\mathcal{F}_K$ denoting the set of faces of K, $\overline{\beta}_F$ and $\overline{\chi}_F$ denote the average of the corresponding quantities on the adjacent elements to the face F and $[\![\cdot]\!]_F$ is the jump of a quantity across F . Considering the vector potential equation for a fixed time step, χ is related to the inverse of the permeability and β corresponds to the electrical conductivity scaled by the time step size. The right hand side $\boldsymbol{f}$ consist of the impressed current $\boldsymbol{J}_{\mathrm{src}}$ and of the magnetic vector potential at the previous time step.

Starting from an initial coarse mesh, we obtain a computational mesh that resolves the eddy current region quite accurate within a few iterations of the adaptive algorithm. In order to avoid remeshing during the simulation, the adaptive grid is created at the beginning of the simulation and used for the complete heating stage $(t_0, t_1]$. For this, we estimate the error during the computation of the magnetic vector potential by solving a few time steps of the discretized vector potential equation, where the the magnetic permeability is set constant to $\mu = \mu_0$ for the creation of the grid. In this way, the grid reflects also the largest penetration depth $\delta = 1/\sqrt{\pi f \mu \gamma}$ that occur during the heating. The restriction of the adapted mesh to Σ is used for the thermomechanical simulation of the workpiece from time t_1 on.

4. Simulation and experimental verification

4.1. **Experimental setting.** A $200\,\mathrm{kW}$ medium frequency plus $100\,\mathrm{kW}$ high frequency induction hardening machine (from EFD Induction GmbH) with Multi Frequency Concept (MFC) for contour hardening was used for induction hardening of the disc samples and gears. For this investigation a spur-gear with module $m = 2$ was used (Figure 3). The main gear data are summarized in Table 1.

Parameter	
Module	2
Number of teeth	21
Gear width	$8\,\mathrm{mm}$
Tip circle	$47.7\,\mathrm{mm}$
Reference circle	$42.0\,\mathrm{mm}$
Root circle	$38.7\,\mathrm{mm}$

Table 1. Gear data

In initial experiments, discs were used as samples to eliminate the influence of the teeth. To allow a direct comparison with the gear, the discs were manufactured with three different outer diameters according to the tip circle ($47.7\,\mathrm{mm}$), reference circle ($42.0\,\mathrm{mm}$) and root circle ($38.7\,\mathrm{mm}$). The bore

FIGURE 3. Gear geometry

diameter ($20\,\mathrm{mm}$) and the disc width ($8\,\mathrm{mm}$) and the materials condition for the disc variants were kept the same as for the gear.

The gear and the disc samples are shown in Figure 4. All samples were heated by a ring inductor with an inner diameter of $50\,\mathrm{mm}$ and a width of $8\,\mathrm{mm}$. Due to the variation in the outer diameters of the disc samples differences in the coupling distance arise.

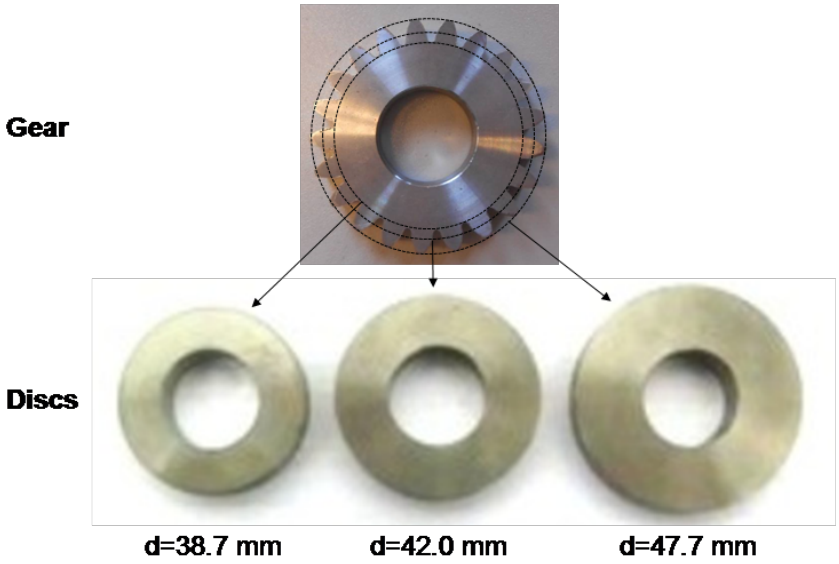

FIGURE 4. Gear and disc samples

For all geometries three different induction heating processes were applied. The samples were either heated with a medium frequency (MF), a high frequency (HF) or supplying simultaneously both frequencies (MF + HF) to the inductor. The frequencies, generator power and current are summarized in Table 2. The heating time was kept constant at $1\,\mathrm{s}$.

[1] power converter current

	MF	HF	MF+HF
Frequency	$12\,\mathrm{kHz}$	$200\,\mathrm{kHz}$	$12\,\mathrm{kHz}/200\,\mathrm{kHz}$
Power	$100\,\mathrm{kW}$	$60\,\mathrm{kW}$	$50\,\mathrm{kW}$ (MF) + $20\,\mathrm{kW}$ (HF)
Current[1]	$575\,\mathrm{A}$	$175\,\mathrm{A}$	$420\,\mathrm{A}$ (MF) + $125\,\mathrm{A}$ (HF)

TABLE 2. Heat treatment variations for disc samples

The samples were heated and subsequently quenched by a shower of a polymer-water mixture. Temperature measurements with pyrometer and thermocouples were performed to obtain the temperature profiles during heating, dwell time (period between heating and quenching) and quenching. The thermocouple is inserted to half disc width from the base of the disc in $1\,\mathrm{mm}$ distance from the surface. The measured temperatures were compared with the simulation.

At selected disc samples the hardness pattern, residual stress and distortion were investigated and compared with simulation results, too. In a further step the attained knowledge from the disc experiments was transferred to the induction hardening of the gears.

Samples for metallographic analyses were taken with water cooled abrasive cut-off machine and then prepared metallographically. Finally they were etched with nital and the hardness pattern was analyzed with a microscope. X-ray diffractometry (XRD) was used for residual stress measurement on discs. The measurements were done based on hardened lateral surface. For in-depth profiles the samples were electro-etched subsequently.

4.2. **Simulation of the induction hardening of discs and comparison with experiments.** Numerical simulations were performed for the disc specimen presented in the last subsection. As described in Section 3, we exploit the symmetry of the workpiece. The middle plane serves as a symmetry plane. In addition, due to rotational symmetry, we only consider a segment of the disc with an angle of $\pi/21$[2].

Induction heating. We simulate the heating procedure of the disc and compare the results to temperature measurements obtained by the experiments described above. The hardening depth given by the experiment is compared to the penetration depth of the martensite phase z_4 obtained after the quenching at time t_{end}.

As a first step, the initial data for the current density has to be defined. In the experiment, the power is specified as relative value in percent. During the experiments it was observed that the corresponding absolute power in kW differs quite a lot for the three disc geometries though the relative value is always the same for medium, high and multi-frequency. It turned out that the measured current is nearly the same for the different coupling distances and is linearly related to the relative power that serves as an input parameter at the machine. This allows us to take the current as input parameter for the simulations. From the specifications of the machine, the transmission ratio between inverter and inductor is known (approx. 9:1 for MF and 10:1 for HF). This gives us an approximate estimate for the inductor current that we use in the simulation.

Due to the different outer diameters of the samples and constant inductor diameter, different coupling distances occurred. Since the energy transfer strongly decreases when this distance increases, the maximum temperature decreased with the outer diameter of the sample, when using the same output power for each frequency variant. This dependency was also shown by the simulation. In Figure 5 the measured and simulated temperatures at the surface of the disc are compared for the heating of the different disc geometries using MF, HF and multifrequency power.

[2]Due to rotational symmetry it is possible to consider the setting in 2D. We are interested in the performance and the calibration of our 3D algorithm and consider a 3D geometry. The angle has been chosen as half the size of a tooth as in the gear experiments.

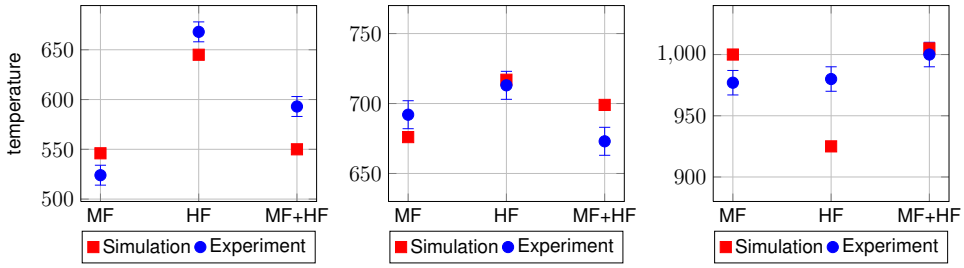

(a) $d = 38.7\,\mathrm{mm}$ (b) $d = 42.0\,\mathrm{mm}$ (c) $d = 47.7\,\mathrm{mm}$

FIGURE 5. Comparison between the measured and simulated temperature for the disc geometries

Temperature profile and hardness pattern. Comparing the experimental results and the simulation, Table 3 and Figure 5, one can see that the temperature is in good correspondence for all disc diameters. The differences are slightly bigger than the measurement error of $\pm 10\,\mathrm{K}$, but in general the temperature is reproduced quite well.

No.	Frequency	Diameter [mm]	Case depth [mm]		Temp. [°C]	
			Sim.	Exp.	Sim.	Exp.
1.	MF	38.7			524	546
2.	HF	38.7			668	645
3.	MF+HF	38.7			593	550
4.	MF	42		0.59	676	692
5.	HF	42	0.54	0.6	717	713
6.	MF+HF	42	0.34	0.16	699	673
7.	MF	47.7	2.43	2.6	1000	977
8.	HF	47.7	1.69	1.94	925	980
9.	MF+HF	47.7	2.17	2.11	1005	1000

TABLE 3. Comparison between simulated (gray) and experimental hardening depth and temperatures

The obtained hardening depth for the experiment and the simulation are also shown in Table 3. In the case of the largest coupling distance, No. 1 to 3, the maximum temperature lay below the austenitization temperature, such that no phase transition could be observed.

For the disc with diameter $d = 42\,\mathrm{mm}$, a phase transition could be observed. In the case of a heating with pure HF and simultaneous MF+HF, experiment No. 5 to 6, the simulated hardening depth lay in the range of the experimentally observed ones. In the case of heating with pure MF, experiment No. 4, the austenitization temperature was not reached in the simulation, while in the experiment a phase transition could be observed and a hardening depth of $0.59\,\mathrm{mm}$ was reached. On the other hand, the simulated temperature lies in a comparable range and is only $20\,\mathrm{K}$ below the experimental result.

One has to mention that the focus was not to fit the simulated temperature to the experimental result. It was the aim to use an input datum that can be reproduced at the machine. It turned out, that the current at the inverter, that can be measured, is related to the relative power that is used as control parameter for the machine. With the knowledge of the transformation ratio between the inverter and the inductor we obtain an estimate of the inductor current, that is used as a source term in the simulation, compare Section 2.4. We obtained the simulation results presented in Table 3, that are in good accordance with the experiments. Especially for the largest disc, experiment No. 7 to 9, which correspond to a realistic coupling distance in induction heating of cylindrical shaped workpieces such as shafts, there is a good

correspondence between experimental and computational result. This holds true for the temperature as well as for the hardening depth.

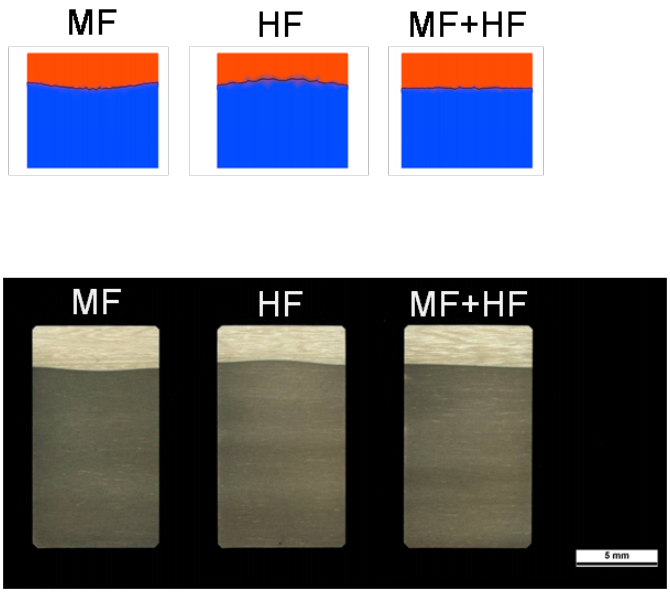

FIGURE 6. Influence of the frequency on the martensitic pattern: simulation and experiment (disc diameter $47.7\,\mathrm{mm}$)

A further indication of the good correspondence is the lateral profile of the martenstic phase fraction. Figure 6 shows a comparison of the simulation and micrograph in longitudinal direction for the biggest disc sample $(47.7\,\mathrm{mm})$ by using different frequencies. In the case of medium frequency, a convex profile with higher penetration depth in the center of the disc could be observed. For HF the profile is concave while for the simultaneous application of medium and high frequency a nearly homogeneous profile could be observed. Especially in the case of HF, the highest temperature can be observed at the edge of the disc. This is for example an important information in order to prevent a melting of the workpiece.

Distortion and residual stresses. The numerical simulations of thermomechanical effects during the cooling period are carried out for discs and gears. The simulations show the temporal and permanent deformation of the workpiece, resulting from temperature, different densities of the various phases and from transformation induced plasticity (TRIP) effects. In [18] we demonstrate that TRIP effects generate distortions of a similar size than the density effects.

The thermomechanical model simulates the size change and the resulting stresses of the discs due to the induction heat treatment. Figure 7 shows the typical distortion of a disc sample after cooling. Due to the phase transformation and TRIP effects, the hardened part of the disc widens in both height and diameter.

Figure 8 shows simulation results for the axial and tangential stresses for the discs with diameter $47.7\,\mathrm{mm}$ for the three induction heating variants. They show that the stress boundary layer gets sharper with the combined frequency treatment.

Figure 9 depicts the comparison of the simulated residual stresses and the experiment carried out on discs with diameter $42\,\mathrm{mm}$ using HF. It shows a very good conformance for the axial stresses.

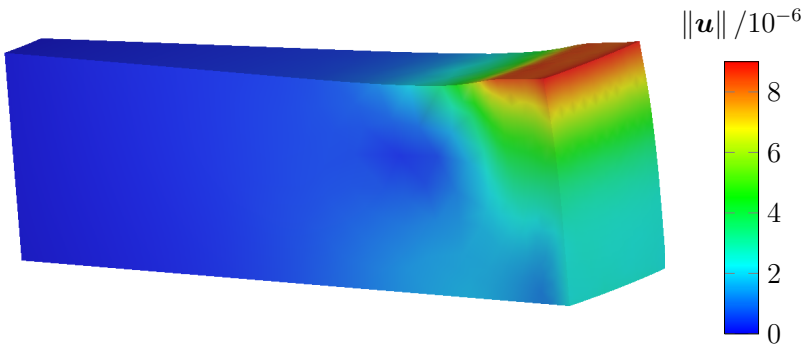

FIGURE 7. Norm of the displacement after cooling using HF with deformation scaled by 40 (disc diameter: $42\,\mathrm{mm}$)

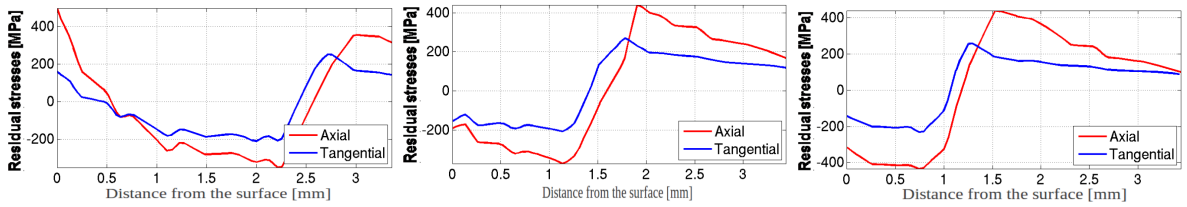

(a) MF (b) HF (c) multi-frequency

FIGURE 8. Axial and tangential residual stresses from simulation for disc diameter $47.7\,\mathrm{mm}$ at the sectional symmetry plane after cooling

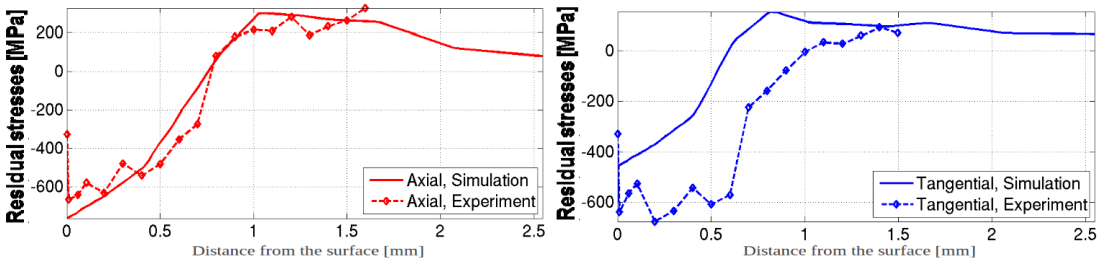

(a) Axial stresses (b) Tangential stresses

FIGURE 9. Axial and tangential residual stresses: Simulation and experiment (disc diameter: $42\,\mathrm{mm}$; heating: HF)

4.3. **Application to gears in an industrial setting.**

4.3.1. *Induction heating, temperature and hardness pattern.* In this section, we present simulations for the contour hardening of a gear using both frequency powers, MF and HF simultaneously. In an industrial setting, very short heating times with high power output are necessary to achieve a contour hardening of gears and to prevent a through hardening of the teeth. An MFC induction hardening machine with higher power output than for the disc specimen was used for the following experiments. The parameters for the contour hardening are shown in Table 4. Both frequencies were supplied simultaneous for $0.25\,\mathrm{s}$ to the inductor.

	MF	HF
Frequency	$10\,\mathrm{kHz}$	$150\,\mathrm{kHz}$
Power	$300\,\mathrm{kW}$	$100\,\mathrm{kW}$
Relative power	$53\,\%$	$22\,\%$

TABLE 4. Parameters for contour hardening of gears

Unfortunately, a measurement of the inductor current or of the inverter current together with the transformation ratio for the MF and HF circuit as in the case of the discs were not available. Since the experiment was done on a different machine it was necessary to calibrate the simulation and to determine the inductor current corresponding to a machine parameter of $100\,\%$ for the MF and HF power.

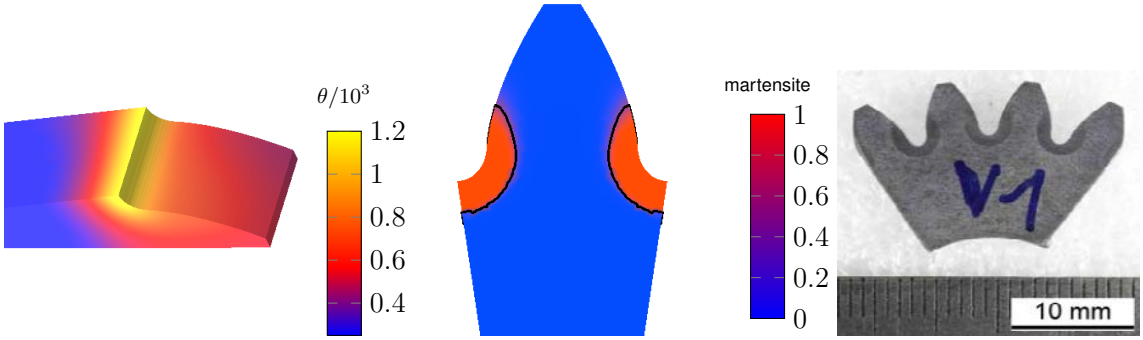

(a) $60\,\%$ MF

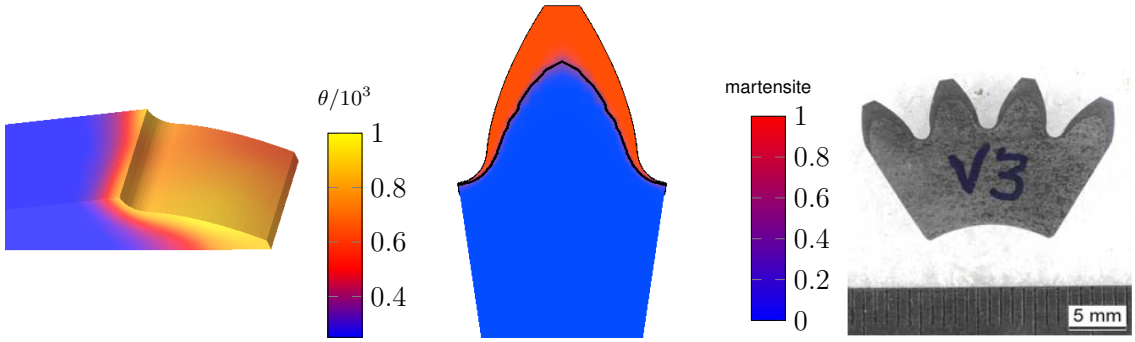

(b) $20\,\%$ MF

FIGURE 10. Calibration of the input parameters for the simulation using experiments with single frequency

To this end, at first experiments using only a single frequency, MF and HF separately, were carried out. By a comparison of polished cross section cut images to simulation results using only a single frequency the input parameters for the simulation were calibrated and the inductor currents corresponding to $100\,\%$ MF- and HF-power were determined. The experimental results using only a single frequency, either MF or HF and the corresponding simulation are shown in Figure 10. Due to the skin effect and the resulting frequency dependent penetration depth a MF shot only hardens the root and the flank of the tooth, while HF only affects the tip of the tooth or even through hardens the tooth, while the fillet and root is not sufficiently hardened.

Having calibrated the input parameters, the simulation with machine specific parameters of $53\,\%$ MF and $22\,\%$ HF was performed without any further adaptation or fitting parameters. The results are shown in Figure 11.

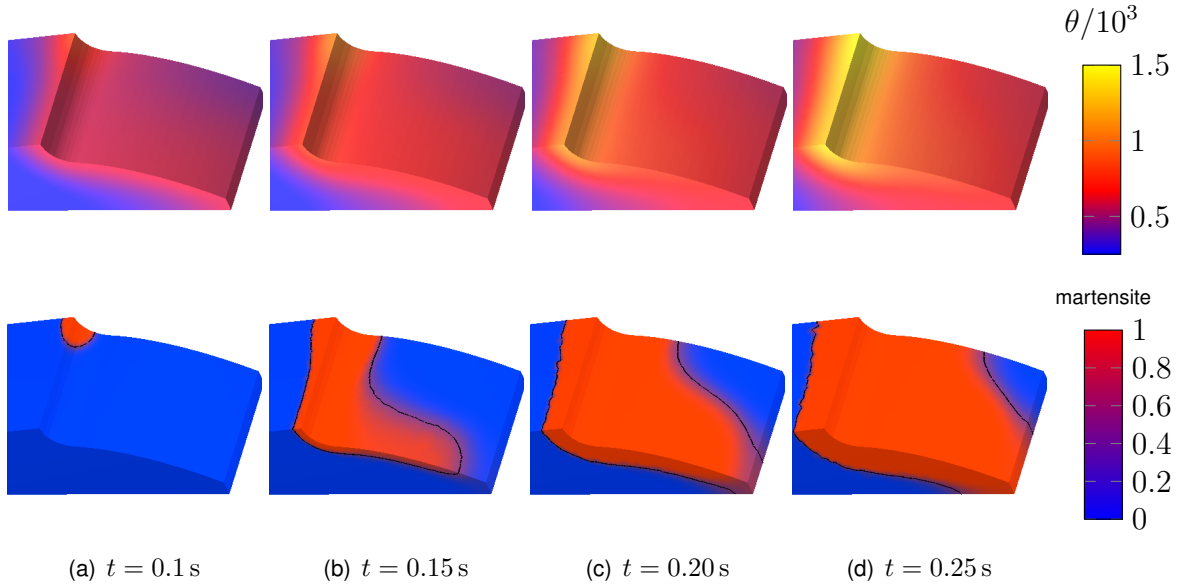

(a) $t = 0.1\,\mathrm{s}$ (b) $t = 0.15\,\mathrm{s}$ (c) $t = 0.20\,\mathrm{s}$ (d) $t = 0.25\,\mathrm{s}$

FIGURE 11. Heating of a gear with the multi-frequency approach

After a heating time of $0.25\,\mathrm{s}$ a contour hardening at the cross section can be observed. The experimental and the simulation results are compared in Figure 12. In the cross section the gear shows a contour hardened profile. But due to “edge effect” this hardness profile is not homogenous over the width of the gear. The simulation gives, by using the parameters mentioned above, the same profile. In addition the hardness profiles on the longitudinal section are compared for the fillet and the tooth. Also on this view there is good accordance between the simulation and the experiment. Even the “edge effects” at the fillet appear in the simulation. To avoid the “edge effect”, the inductor must be optimized.

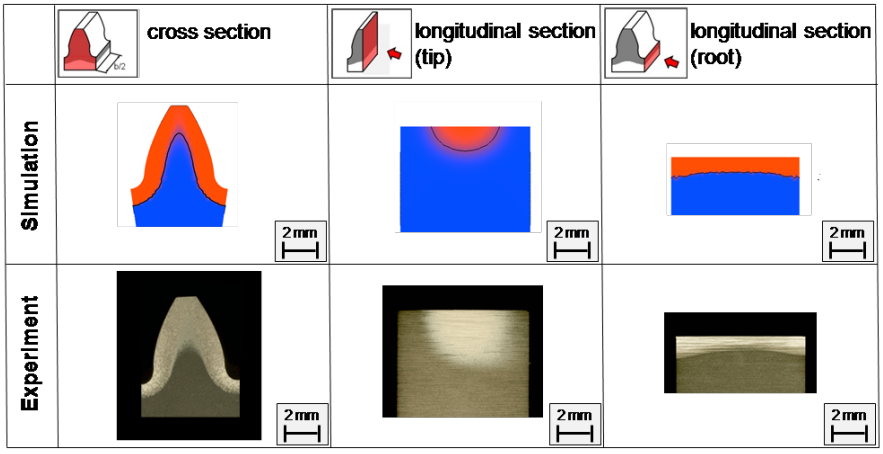

FIGURE 12. Simulated austenite profiles and micrographs from the experiment

4.3.2. *Thermomechanics.* The mechanical properties of gears are very important for the operation and life cycle of the work piece. A hard surface, produced by martensite, prevents plastic deformations at contact, while pearlite, bainite, etc in the interior prevents a brittle behaviour and breaking of teeth. These are the properties produced mainly by the microstructure and phase distribution.

Additionally, the presence of resiual compression stresses near the surface in contact is important for operation, in order to compensate for tensile stresses which are typically generated by the contact of gear wheels.

Finally, also the deformation of the gear wheel after heat treatment is important, as distortions larger than a tolerance generate an additional production step of grinding.

Thus, we analyze here the mechanical deformation and residual stresses for the gear wheels. In Figure 13, we show the deformations during the cooling phase, together with the temporal evolution of the phase transformation. Due to the strong cooling, all austenite is transformed to martensite. The final deformation is shown in more detail in Figure 14. This final deformation is not only due to the phase distribution and corresponding inhomogeneous density distribution, but TRIP effects are quite important, too. A similar simulation without using the TRIP model gives quite different deformations and distribution of residual stresses, see [18].

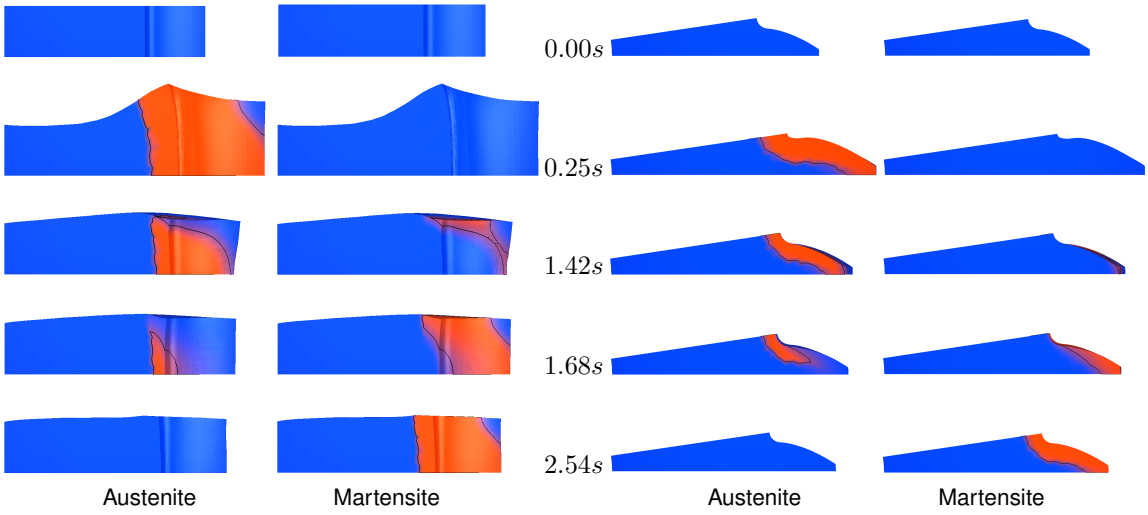

FIGURE 13. Evolution of austenite and martensite shown from tooth flank (left) and from gear middle plane (right) with deformation scaled by 40

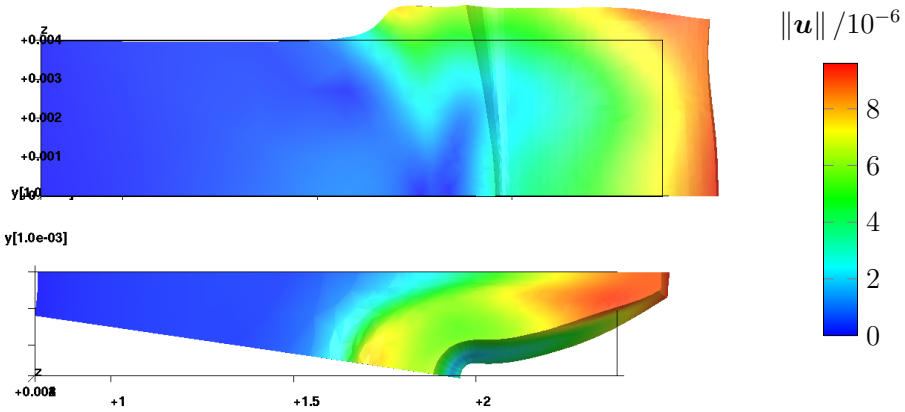

FIGURE 14. Norm of the displacement after cooling with deformation scaled by 150

The residual stresses after the heat treatment are computed and shown at the tip, the root of the gear, and near the root in a normal direction of 30 degrees, see Figures 15 and 16.

The figures clearly show residual compression stresses near the gear root and the 30 degree position, with a depth of about 1mm. For the gear tip, tangential stresses are slightly compressive up to a depth of 2mm, while axial ones are not. This is in correspondance to the results from the disc simulation, where a deeper hardening produces less (or even no) compressive stresses near the surface. For the use of the gear wheel, the compressive stresses near the root area are able to compensate for tensile stresses produced by the contact of gears. Presumably, a less deep hardening profile near the gear tip or an otherwise different heat treatment would be needed in order to produce compressive stresses also there.

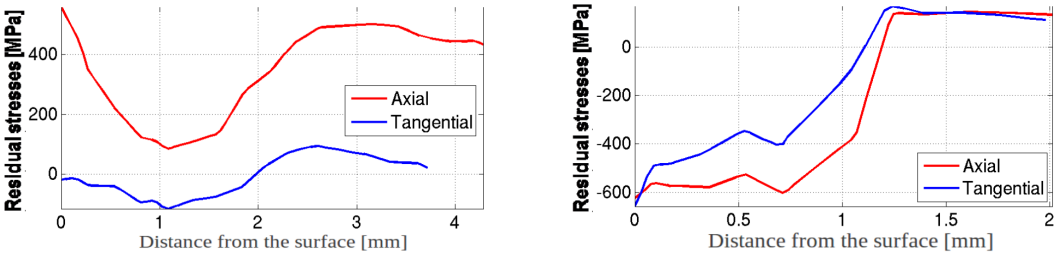

FIGURE 15. Axial and tangential residual stress from gear tip (left) and root (right) towards the center of the gear

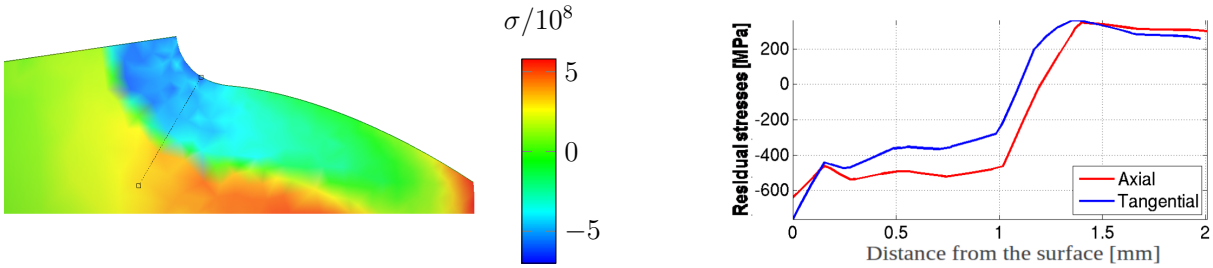

FIGURE 16. Geometry with axial stress on a cross section (left), and axial and tangential stress along the direction with angle of $\pi/6$ (right)

5. CONCLUSION

In the present paper a electro-thermo-mechanical mathematical model of multi-frequency induction hardening has been presented together with an efficient simulation approach. Key features are adaptive finite elements in space, and a time discretization with different time scales for the electro-magnetic and the thermomechanical part, respectively. The necessary material parameters have been taken from literature supported by additional measurements. To validate the simulations experiments have been conducted.

Despite the fact that no fitting of data has been done, the experiments are in excellent agreement with the numerical results. In a second verification step, experiments at an industrial partner have been conducted. Since in that case no current measurements were available the input parameters were calibrated for 100% MF- and HF-power, respectively. Then a multi-frequency simulation has been done with the frequency fractions specified by the company. The resulting simulation results showed a nice contour-hardened pattern and were again in excellent agreement with the experiments.

In view of these results it is fair to say that a new, efficient and experimentally validated simulation tool for multi-frequency hardening has been developed. The next step will be the application of this tool to more important components, such as helical and bevel gears. Another promising aim of future research is to study the related optimal control problem. For a first approach in this direction we refer to [3].

REFERENCES

[1] Rudi Beck, Ralf Hiptmair, Ronald HW Hoppe, and Barbara Wohlmuth. Residual based a posteriori error estimators for eddy current computation. *ESAIM: Mathematical Modelling and Numerical Analysis*, 34(01):159–182, 2000.

[2] K. Berggren and H. Stiele. Induction heating: A guide to the process and its benefits. *Gear Solutions*, 10(7):40–46, 2012.

[3] Oleg Boyarkin and Ronald H. W. Hoppe. Optimal control of inductive heating of ferromagnetic materials. *Russian Journal of Numerical Analysis and Mathematical Modelling*, 28(6):519–546, 2013.

[4] S Clain, J Rappaz, M Swierkosz, and R Touzani. Numerical modeling of induction heating for two-dimensional geometries. *Mathematical models and methods in applied sciences*, 3(06):805–822, 1993.

[5] F. D. Fischer, G. Reisner, E. Werner, , K. Tanaka, G. Cailletaud, and T. Antretter. A new view on transformation induced plasticity (trip). *Int. J. Plast.*, 16(0):723 – 748, 2000.

[6] F. D. Fischer, Q. P. Sun, and K. Tanaka. Transformation-induced plasticity (trip). *Int. J. Plast.*, 49(0):317 – 364, 1996.

[7] M. Hahn, H. Autenrieth, O. Meyer, A. Schulz, and H. W. Zoch. Experimentelle und numerische untersuchung zum induktiven vorschubhärten von profil führungsschienen. *HTM Journal of Heat Treatment and Materials*, 67(6):366–377, 2013/11/14 2012.

[8] Sofia Hansson and Martin Fisk. Simulations and measurements of combined induction heating and extrusion processes. *Finite elements in analysis and design*, 46(10):905–915, 2010.

[9] F. Hegewaldt. Vorausbestimmung der Einhärtungstiefe beim induktiven Oberflächenhärten. *Härterei-Tech. Mitt.*, 17(2):75–81, 1962.

[10] Dietmar Hömberg. A mathematical model for induction hardening including mechanical effects. *Nonlinear Analysis: Real World Applications*, 5(1):55–90, 2 2004.

[11] Dietmar Hömberg, Thomas Petzold, and Elisabetta Rocca. Analysis and simulations of multifrequency induction hardening. *Nonlinear Analysis: Real World Applications*, 22:84–97, 2015.

[12] John D. Jackson. *Classical Electrodynamics Third Edition*. Wiley, third edition, 1998.

[13] Dimitris Labridis and Petros Dokopoulos. Calculation of eddy current losses in nonlinear ferromagnetic materials. *Magnetics, IEEE Transactions on*, 25(3):2665–2669, 1989.

[14] J.-B. Leblond, J. Devaux, and J. C. Devaux. Mathematical modelling of transformation plasticity in steels. i: Case of ideal-plastic phases. *Appl. Mech. Rev.*, 5(0):551 – 572, 1989.

[15] I. Magnabosco, P. Ferro, A. Tiziani, and F. Bonollo. Induction heat treatment of a iso c45 steel bar: Experimental and numerical analysis. *Computational Materials Science*, 35(2):98–106, 2 2006.

[16] Leif Markegard and Wolfgang Schwenk. Method and device for surface hardening of rotation symmetrical parts through inductive heating by means of at least two different frequencies. *European Patent*, 91906813(EP 0524207 B1), 1991/04/05 1995.

[17] Peter Monk. *Finite Element Methods for Maxwell's Equations (Numerical Analysis and Scientific Computation Series)*. Oxford University Press, USA, 2003.

[18] Jonathan Montalvo-Urquizo, Qingzhe Liu, and Alfred Schmidt. Simulation of quenching involved in induction hardening including mechanical effects. *Computational Materials Science*, 79(0):639 – 649, 2013.

[19] J. C. Nédélec. Mixed finite elements in R^3. *Numerische Mathematik*, 35(3):315–341, 09 1980.

[20] Jörg Ostrowski. *Boundary Element Methods for Inductive Hardening*. PhD thesis, Eberhard-Karls-Universität zu Tübingen, 2003.

[21] Thomas Petzold. *Modelling, Analysis and Simulation of Multifrequency Induction Hardening*. PhD thesis, Technische Universität Berlin, 2014.

[22] Dirk Schlesselmann and Bernd Nacke. Anwendungen der numerischen Simulation des induktiven Randschichthärtens. *Elektrowärme International*, 71(3):89–94, 2013.

[23] Maximilian Schwenk. *Entwicklung und Validierung eines numerischen Simulationsmodells zur Beschreibung der induktiven Ein- und Zweifrequenzrandschichthärtung am Beispiel von vergütetem 42CrMo4*. PhD thesis, Karlsruher Institut für Technologie (KIT), 2012.

[24] L. Taleb and F. Sidoroff. A micromechanical modeling of the greenwood-johnson mechanism in transformation-induced plasticity. *Int. J. Plast.*, 19(0):1821 – 1842, 2003.

[25] Rüdiger Verfürth. *A Posteriori Error Estimation Techniques for Finite Element Methods*. Oxford University Press, 2013.

[26] E. Wrona. *Numerische Simulation des Erwärmungsprozesses für das induktive Randschichthärten komplexer Geometrien*. PhD thesis, Universität Hannover (ETP), Cuvillier Verlag, Göttingen, 2005.

[27] E. Wrona, B. Nacke, and D. Resetov. 3d-modelling of the transient heating process for induction surface hardening. In *Int. Sci. Colloq.; Modelling for Electromagnetic Processing, Hannover, March 24-26*, pages 119–123, 2003.